# Resilience for Cyber-Physical Energy Systems

Deliverable D1.2

# Final Public Report

Version 1.0

Deliverable

Filip Pröstl Andrén (AIT)
Arlena Wellßow (OFFIS), Henrik Sandberg (KTH), Daniel Selvaratnam (KTH), Marco Mittelsdorf (ISE), Denis Vettoretti (AIT), Diego Cifelli (AIT), Catalin Gavriluta (AIT)

2025-05-27

This project has received funding in the framework of the joint programming initiative ERA-Net Smart Energy Systems' focus initiative Digital Transformation for the Energy Transition, with support from the European Union's Horizon 2020 research and innovation programme under grant agreement No 883973.

Smart
Energy
Systems
ERA-Net

## DOCUMENT INFORMATION

| | |
|---|---|
| • **Deliverable No.:** | D1.2 |
| • **Deliverable Name:** | Final Public Report |
| • **Work Package:** | WP1 Project Coordination and Management |
| • **Lead Partner:** | AIT |
| • **Submission Date:** | 2025-05-27 |
| • **Status:** | ☐ draft, ☐ final, ☒ submitted |

## DISSEMINATION LEVEL

| | | |
|---|---|---|
| ☒ | **Public** | Publicly available |
| ☐ | **Programme Participants** | Restricted to other programme participants (including ERA-Net and national funding organizations) |
| ☐ | **Restricted** | Restricted to a group specified by the Consortium (including ERA-Net and national funding organizations) |
| ☐ | **Confidential** | Confidential, only for members of the Consortium (including ERA-Net and national funding organizations) |

## CHANGE LOG

| Date | Version | Author/Editor | Summary of Changes Made |
|---|---|---|---|
| 2022-09-15 | v0.1 | F. Pröstl Andrén (AIT) | Initial document structure |
| 2025-05-26 | v0.2 | F. Pröstl Andrén (AIT) | Added section on AI tools |
| 2025-05-27 | v1.0 | F. Pröstl Andrén (AIT) | Final inputs |

# TABLE OF CONTENTS

# 1 Executive Summary

The RESili8 project addresses the urgent need for a reimagined approach to resilience in Cyber-Physical Energy Systems (CPESs), particularly in the context of the digital transformation of the energy sector. Traditional resilience strategies, such as over-provisioning and physical redundancy, are no longer sufficient to manage the increasing complexity, decentralization, and cyber-physical interdependencies of modern energy infrastructures. RESili8 proposes a novel solution package that integrates AI-based analysis, sustainable planning, and continuous validation to ensure secure, efficient, and adaptive energy system operation.

One important part of the project is the development of an AI-based resilience analysis toolchain that combines expert knowledge with machine learning techniques. This toolchain leverages System Theoretic Process Analysis (STPA), Misuse Case (MUC) modeling, and Holistic Test Descriptions (HTDs) to generate realistic and test cases. These test cases are used to train reinforcement learning agents, enabling the identification of critical threat scenarios and the generation of reproducible lab tests. The approach accelerates the development and validation of resilient energy applications.

To support the rapid and scalable validation of smart grid applications, RESili8 introduces the Automated Cyber-Physical Testing and Validation Framework (ACTV). It extends modern CI/CD pipelines by integrating system-level validation capabilities, allowing developers to test their applications in real-time simulation environments. ACTV supports modularity, reusability, and distributed collaboration, making it a powerful tool for validating complex software ecosystems in the energy domain.

The project demonstrates the effectiveness of ACTV through a use case involving smart electric vehicle (EV) charging. Using the CIGRE low-voltage distribution network as a benchmark, the validation pipeline automates the deployment and testing of energy management systems (EMS) and control algorithms. The results show that the EMS can successfully adapt to dynamic grid constraints, maintaining power consumption within defined limits while optimizing EV charging behavior.

Another major focus of RESili8 is fault localization in heterogeneous distribution grids. The project evaluates three complementary methods: ElectroMagnetic Time Reversal (EMTR), Lumped Parameter Single Feeder (LPSF), and a Partial Differential Equation (PDE)-based approach. Each method is tested using both simulated and real-world data, with results highlighting their respective strengths and limitations. EMTR offers high accuracy but is sensitive to network heterogeneity; LPSF is lightweight but less robust in complex scenarios; and the PDE method provides high-fidelity modeling for theoretical and feasibility studies.

The integration of these fault localization techniques enhances resilience by enabling early detection and precise localization of faults, which is critical for minimizing downtime and improving system reliability. The project also explores the use of data-driven and model-based estimators to improve fault detection accuracy, particularly in high-ohmic and complex network conditions.

RESili8's contributions extend beyond technical innovations to include methodological advancements and collaborative practices. The project emphasizes the importance of combining expert knowledge with AI, automating validation processes, and fostering cross-disciplinary collaboration. These principles are essential for building resilient energy systems that can adapt to evolving threats and operational challenges.

The outcomes of RESili8 are validated through extensive simulations, lab testing, and real-world data analysis. The project's tools and frameworks are designed to be scalable, interoperable, and adaptable to a wide range of energy system configurations. This ensures that the solutions developed are not only effective in controlled environments but also applicable in diverse real-world contexts.

In summary, RESili8 delivers a comprehensive and forward-looking approach to resilience in CPESs. By integrating AI-driven analysis, automated validation, and advanced fault localization, the project sets a new standard for resilience engineering in the energy sector. Its results provide a solid foundation for future research, development, and deployment of secure, intelligent, and sustainable energy systems.

# 2 Introduction

The transformation of energy systems into highly digitalized, interconnected infrastructures has introduced unprecedented complexity and vulnerability. Traditional approaches to ensuring resilience—such as over-provisioning and redundancy—are increasingly inadequate in the face of evolving cyber-physical threats, distributed energy resources (DERs), and the integration of intelligent control systems. The RESili8 project addresses this challenge by proposing a novel resilience solution package tailored for Cyber-Physical Energy Systems (CPESs). This package integrates AI-based analysis, sustainable planning, and continuous validation to support the secure and efficient operation of future energy systems.

The core motivation behind RESili8 is the recognition that resilience must be redefined for the digital age. Rather than relying solely on physical redundancy, the project emphasizes intelligent, adaptive, and proactive strategies that leverage expert knowledge, machine learning, and real-time testing. This shift is essential to accommodate the increasing penetration of renewable energy sources, the rise of prosumers, and the growing interdependence between information and operational technologies in the energy domain.

RESili8 brings together leading European research institutions, industry partners, and need-owners to co-develop and validate its resilience framework. The project's methodology is grounded in a multi-layered approach that spans from conceptual modeling and AI-driven threat analysis to hardware-in-the-loop (HIL) testing and real-world pilot demonstrations. This comprehensive scope ensures that the proposed solutions are not only theoretically sound but also practically viable and scalable.

A key innovation of the project lies in its AI-based resilience analysis toolchain, which combines System Theoretic Process Analysis (STPA), Misuse Case (MUC) modeling, and Holistic Test Descriptions (HTDs). This toolchain enables the generation of realistic, high-impact test cases for lab validation, significantly accelerating the development and deployment of resilient energy applications. Reinforcement learning techniques are employed to explore and evaluate complex threat scenarios, enhancing the robustness of the resulting models.

In parallel, RESili8 introduces an Automated Cyber-Physical Testing and Validation Framework (ACTV) that integrates seamlessly with modern CI/CD pipelines. This framework supports scalable, distributed testing of smart grid applications, bridging the gap between offline simulations and real-time field validation. By enabling continuous integration of resilience testing into the software development lifecycle, ACTV fosters a culture of proactive resilience engineering.

The project also explores advanced fault localization techniques for heterogeneous distribution grids, comparing methods such as ElectroMagnetic Time Reversal (EMTR), Lumped Parameter Single Feeder (LPSF), and Partial Differential Equation (PDE)-based modeling. These methods are evaluated through simulations and real-world data to assess their effectiveness in detecting and localizing faults under varying conditions.

Together, these innovations position RESili8 as a pioneering initiative in the field of energy resilience. By combining theoretical rigor with practical implementation, the project aims to lay the groundwork for a new generation of resilient, intelligent, and sustainable energy systems.

The rest of the document is structured as follows: Section 3 provides an overview of the AI-based resilience analysis toolchain, Section 4 describes the rapid development and validation framework and Section 5 provides an overview of the three different fault localization methods developed in the project. Finally, conclusions are provided in Section 6.

# 3 AI-Based Resilience Analysis: From Expert Knowledge to Test Case Generation

The convergence of the energy grid, a critical national infrastructure known as the smart grid, from both IT and OT perspectives necessitates the inclusion of expertise from grid operators and ICT specialists. This is crucial due to the implementation of ICT-based control systems, which are integrated into the grid to manage volatile generation and prosumers efficiently. While enhancing usability, this integration also introduces a heightened risk of errors and potential cyber attacks, consequently increasing the likelihood of system failure [7, 25, 32].

Traditionally, the risk of failure within the energy system was mitigated by the redundancy of the physical system (following the N-1 rule) [7]. However, with the growing need for highly efficient power grid operation, driven by extensive ICT integration, this approach is no longer sufficient. The integration of ICT introduces its own set of risks, where the failure of physical systems can lead to the failure of ICT systems and vice versa. Redundancy remains important, but it alone cannot address these risks; new technologies such as secure communication protocols and encryption must be employed for mitigation [25, 32].

The power grid is transforming, rendering it highly non-deterministic as an overall system. The complexity arises from the introduction of machine learning systems for optimization, the proliferation of prosumer roles, the emergence of localized energy markets, and the significant contribution of distributed renewable energy sources (DERs) in achieving efficiency goals. Extensive simulations are required to develop mitigations in response to these challenges [39, 40].

RESili8 contributes to this development by adding new approaches for the resilient operation of energy systems as well as optimal and sustainable planning, AI-based analysis of resilient architectures, and continuous implementation and validation of resilient applications.

In this work, we focus on developing fundamental methods that are essential for using threat and hazard analysis to improve the learning capability of AI-based models. This comprehensive effort includes developing and refining a specialized analysis tool based on Deep Reinforcement Learning (DRL). The planned outcomes of this project will manifest themselves in the form of carefully crafted formats suitable for human understanding and machine interpretation. These formats will play a central role in facilitating model training processes and enable seamless integration with the intricate nuances of AI-based learning methods.

Another critical aspect of the planned deliverables concerns the provision of datasets that serve as a robust training and testing environment and thus contribute significantly to the iterative refinement and validation of the developed AI models. Essentially, this work package is intended to contribute to the convergence of threat and hazard analysis with state-of-the-art AI technologies and create a symbiotic relationship between analytical findings and machine intelligence.

Here, we present a novel approach by combining System Theoretic Process Analysis (STPA) with Misuse Case (MUC) templates as well as Holistic Test Descriptions (HTD) to accomplish a toolchain that, with reinforcement learning embedding, analyses possible threat situations even further and in more detail. This allows faster test case generation for lab-based testing, as the output of this toolchain are lab specifications of explicit test cases. While STPA and MUCs enable expert knowledge input into reinforcement learning experiments, the machine learning part in this toolchain allows checking multiple parameters and set-ups faster than possible in a real-time lab. The situations labeled as especially critical after training and testing the reinforcement learning agents are then described in HTD to allow a reproducible lab test.

## 3.1 Knowledge Representation for AI-Based Models

During the RESili8 project, we conceptualized a comprehensive toolchain that begins with System Theoretic Process Analysis (STPA), followed by AI experiment execution and test description. This toolchain is designed to assist software developers in the energy sector in identifying edge-test cases for their software. These test cases contain all necessary information for the specific test environment and its configuration.

Our approach integrates Misuse Case (MUC), Systems Theoretic Process Analysis (STPA), and Holistic Test Description (HTD) in a hierarchical manner, as detailed in a previous deliverable published at the first nfdi4energy conference [43]. This hierarchical structure enables a systematic and comprehensive analysis of complex systems, as illustrated in Figure 1.

At the initial level, we apply STPA to the topic of interest, yielding hazard scenarios that identify potential risks and vulnerabilities. These scenarios serve as input to define MUCs, which provide a detailed description of the situation, including relevant actors, goals, and constraints. The MUCs are refined through expert knowledge, incorporating domain-specific information and nuances to ensure a thorough understanding of the system.

From these MUCs, experiments can be designed either directly from the MUC data or by combining multiple data formats. This flexible approach allows for the creation of tailored experiments that address specific research questions and objectives.

Our concept extends the MUC-STPA toolchain with HTD for test definition, particularly useful in lab testing where controlled environments can simulate real-world scenarios. This addition enhances the toolchain, allowing critical scenarios identified through reinforcement learning experiments to be evaluated in a laboratory setting with real-time operating components. This enables researchers to validate their findings and refine their models in a more realistic and dynamic environment.

Furthermore, integrating STIX and TAXII into this concept enables the creation of a shareable knowledge database that can be expanded upon receipt of analysis results. This facilitates collaboration and knowledge sharing among stakeholders, allowing for the aggregation of expertise and the development of more comprehensive and accurate models. The resulting database serves as a valuable resource for future research, providing a foundation for further analysis and experimentation.

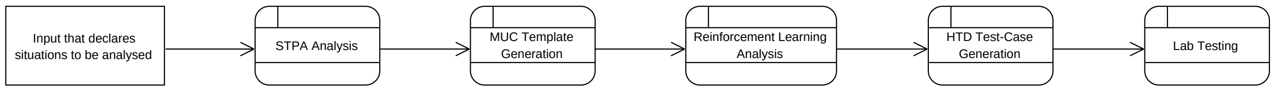

Figure 1: Information flow for the proposed concept.

## 3.2 Example Scenario and AI Analysis

To validate our concept and raise the technology readiness level, we selected a representative scenario from the RESili8 project involving electric vehicle (EV) charging. This scenario, relevant to both the project and its industrial partners, considers the impact of controllable and uncontrollable wall boxes from the perspective of a Distribution System Operator (DSO). We based our analysis on the Cigre-LV-grid, which is also used in the project's rapid validation phase, ensuring consistency in specifications and relevance for test case generation.

After identifying potentially harmful control actions within this grid, we initiated an AI-based analysis. The process began with the creation of a misuse case, developed through expert interviews [46]. The misuse case helped define specific scenarios and was used to generate a structured AI experiment using the palaestrAI framework, which employs reinforcement learning and adversarial resilience learning (RL-ARL). A state machine was derived from the misuse case to simulate the scenario and guide the learning process. These state machines, published in prior work [45], were designed to generate data for training and testing agents.

---

[1] `https://pandapower.readthedocs.io/en/v2.1.0/networks/cigre.html#low-voltage-distribution-network`

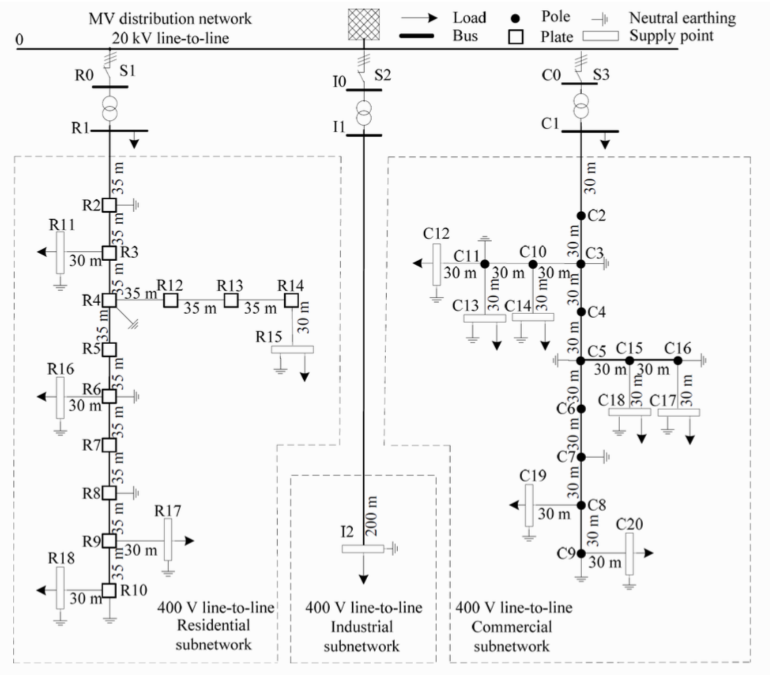

Figure 2: CIGRE Low Voltage Distribution Network [1]

Once the experiment design and state machines were finalized, we executed the experiments using the arsenAI submodule of palaestrAI [46]. This tool automated the setup, including environment configuration, agent initialization, and the orchestration of training and testing phases. Initially, scenario-specific data was generated, followed by agent training and evaluation to determine whether the agents could replicate the encoded strategies. The results are seen in Figure 3 and in Figure 4.

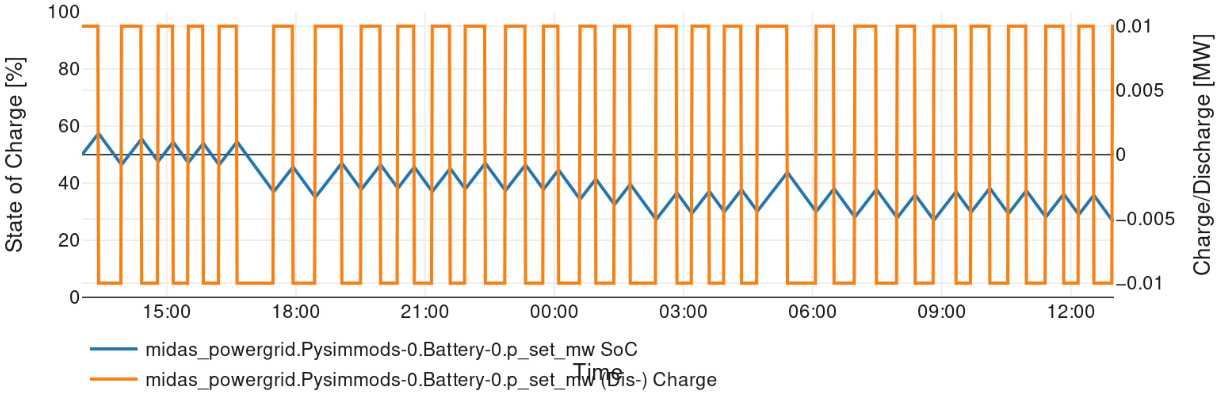

Figure 3: Data Generated by the State Machine. The blue line shows the state of charge of the controlled battery and is connected to the left y-axis, while the orange line shows the setpoints given for the battery on the right y-axis from maximal discharge to maximal charge for this battery.

Our analysis revealed that agents trained with data reflecting specific strategies could successfully reproduce those strategies, even when guided by general objectives. While online, hybrid, and offline training modes yielded similar results [44], the simplicity of the medium-voltage grid limited the impact of agent actions. Consequently, we transitioned to the low-voltage Cigre benchmark grid, which better suited the project's offline learning goals.

The experiment data was stored in a hierarchical SQL database and could be accessed using the Python-based CLI tool *palaestrAI database query* (paldaque). This utility allows users to query and export data, including agent-generated setpoints, in CSV format. These outputs can be used in

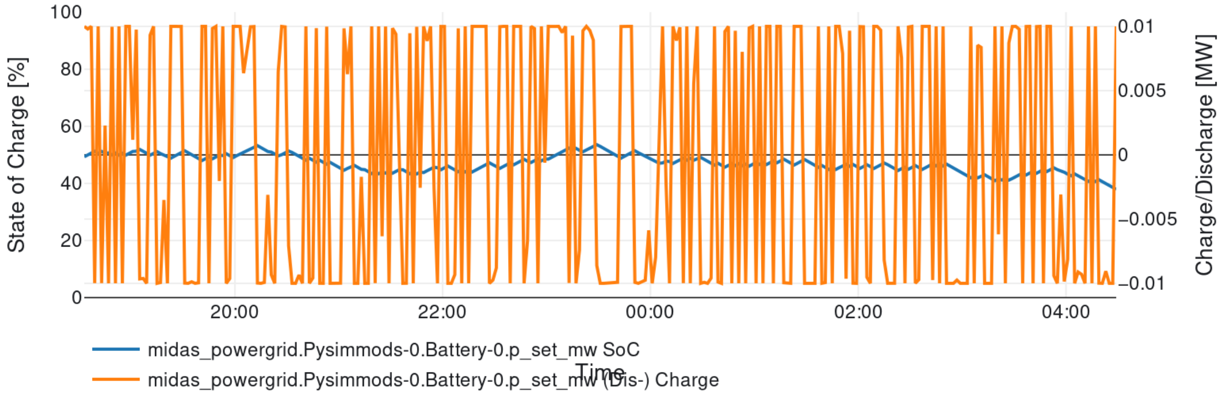

Figure 4: Learned Battery Settings after Hybrid Training. The blue line shows the state of charge of the controlled battery and is connected to the left y-axis, while the orange line shows the setpoints given for the battery on the right y-axis from maximal discharge to maximal charge for this battery.

physical simulations of the benchmark grid to evaluate new algorithms and hardware under worst- and best-case scenarios. Additionally, identified vulnerabilities can be shared using standardized formats like STIX/TAXII.

The prototype we developed supports a semi-automated toolchain, beginning with manual scenario analysis and progressing through automated data generation and agent training, ending with manual data export for lab testing. Our findings showed that synchronizing external grid and battery setpoints led to the most unstable grid conditions, offering the highest reward for an attacker. However, a battery size of 0.01 MW was insufficient to cause significant disruption alone, indicating the need for larger simulated batteries in critical test cases. Notably, even with general objectives, agents were able to follow the strategies embedded in the training data, as seen in Figure 5.

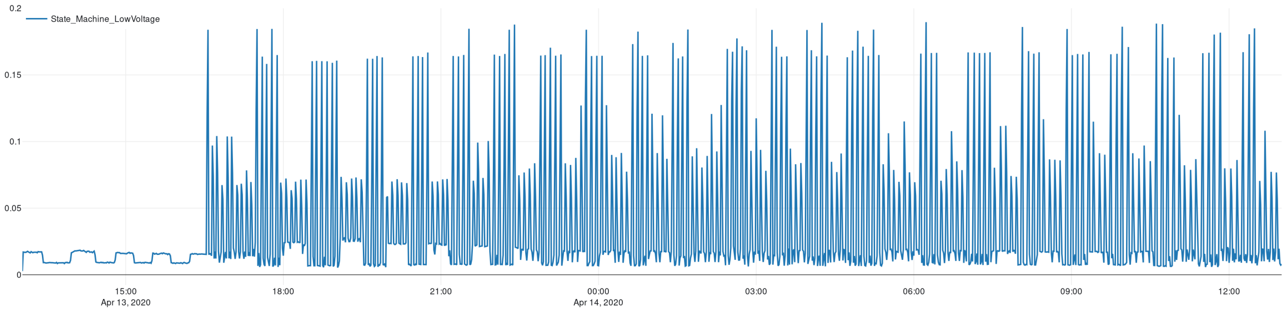

Figure 5: Objective Value Generated by the State Machine. High Values show a good performance for the action taken. The state machine generates good and bad rewards for the agent to learn from.

# 4 Rapid Development and Validation of Smart Grid Applications

The massive deployment of distributed generators from renewable sources in recent years has led to a fundamental paradigm change in terms of planning and operation of the electric power system. Automation and control systems, using advanced information and communication technology, are key elements to handle these new challenges. To counteract the increased complexity associated with this change, new engineering and validation methods are needed [49], [6]. However, these methods mainly focus on traditional offline and component validation, not taking the whole system into account. Previously there used to be a large gap between offline simulations and laboratory prototypes, a gap that would make iterating between design and testing a slow and costly process. However, this has been addressed nowadays by the advancements in Real-time Digital Simulators (RTDSs). Performing intermediate Hardware-in-the-Loop (HIL) tests in the form of Controller-HIL (C-HIL), Power-HIL (P-HIL), or both, has become the state of the art [22].

The advantages of using RTDSs and HIL tests for the validation of component-level applications are uncontested. Unfortunately, the same cannot be said when analysing the available options for validating large-scale distributed software ecosystems operating in the context of an increasingly digitalized power system. Thus, real-time execution and simulation of cyber-physical systems are gathering interest in the field of large-scale digitalized electrical power systems [5], [48]. Digitalization is widely seen in the field as a source of opportunities and benefits, yet it also presents challenges and complexities. On the one hand, it has the potential to solve a lot of the existing problems through intelligent coordination of distributed resources, but on the other hand, it opens the door to serious cyber-security threats.

The transition towards massively distributed software applications interacting with the critical electrical energy supply infrastructure is already on its way. However, current tools and methodologies are not suitable to systematically test and validate the system impact of these applications before deployment. Adhoc approaches built around real-time (RT) [12], [27] simulation platforms can be found in the literature; however, they all suffer from scalability and interoperability issues. Some approaches based on co-simulation [24] for system-level testing exist. However, existing approaches have one of two things in common. Either they focus primarily on the power system domain and leave any integration of software applications up to the user. Or, if they cover both domains, they are developed and configured manually for a specific application, where changing the testing scenario or adding more components to the system requires considerable effort and the risk of introducing manual errors increases. Until now, a methodology for system-level testing that provides tool support for scaling and configuring cyber-physical energy systems.

As the complexity of scenarios emerging in the context of highly digitalized electrical power systems continues to increase, proper test coverage becomes a real challenge. Therefore, as the number of tests required to provide good test coverage grows exponentially, and the models and generated data start to grow beyond the reasonable scope of manual inspection, researchers and engineers will need to rely more heavily on automation in these processes.

## 4.1 Automated Cyber-Physical Testing and Validation Framework

Automated testing is a cornerstone of modern software engineering, encompassing unit to system-level tests. Continuous integration (CI) and continuous deployment (CD) pipelines further streamline the build, test, and release cycle, enabling rapid feedback and efficient delivery. Integrating automated testing into the development lifecycle helps detect issues early, reducing costs across the product lifecycle [18]. It also fosters confident iteration and ensures high-quality software that meets stakeholder expectations—especially critical in domains like electrical power systems.

The proposed Automated Cyber-Physical Testing and Validation Framework (ACTV) enhances traditional CI/CD pipelines by incorporating as-a-service tools for seamless cyber-physical integration

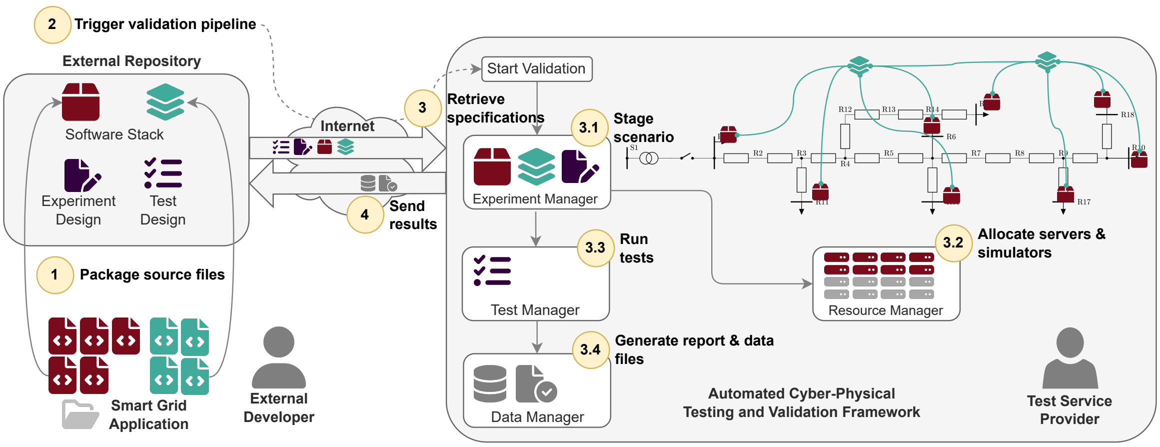

Figure 6: Automated Cyber-Physical Testing and Validation Framework.

testing. It is built on five core principles: modularity, reusability, reproducibility, language-agnosticism, and interoperability, with a focus on:

1. *Efficiency*: Streamlined configuration and parallel test execution.
2. *Scalability and flexibility*: Support for diverse power system models, evolving requirements, and adaptable interfaces.
3. *Automation*: Minimization of manual tasks to accelerate validation.
4. *Distributed collaboration*: Support for geographically distributed testing and shared resources like RT simulators.

ACTV bridges the gap between offline simulations and field testing for system-level validation. It adopts a controller-software-in-the-loop (C-SIL) approach—deploying control algorithms as software rather than hardware—enabling scalable, hardware-independent testing. This allows comprehensive validation of critical infrastructure software alongside the systems they control.

Figure 6 illustrates the ACTV workflow. After passing standard software tests, a developer packages the application and pushes it to the active repository (Step 1). Alongside the software, the developer provides:

- *Experiment Design (ED)*: Describes the physical system and software integration.
- *Test Design (TD)*: Specifies cyber-physical test scenarios.

The remote validation pipeline is then triggered (Step 2). In Step 3, the system fetches the software and test specifications. The Experiment Manager uses the ED to generate simulation models and interface configurations (Step 3.1), and allocates computational resources (Step 3.2). The scenario is deployed, and the Test Manager executes the tests (Step 3.3), collects data, and generates reports (Step 3.4).

All tests are conducted at the Test Service Provider (TSP) site, independently of the developer. The TSP manages the test environment and schedules execution based on resource availability. Upon completion, results and datasets are returned to the developer for analysis.

## 4.2 Rapid Development and Validation Pipeline Prototype

Building on the ACTV concept, a prototype was developed to integrate with CI/CD platforms like GitLab and GitHub. These platforms automate software build, test, and deployment processes. The ACTV framework extends this by attaching validation steps to the CI/CD pipeline, integrated into an existing GitLab pipeline.

Figure 7 illustrates the validation pipeline, comprising three components: the development pipeline (yellow), the extended pipeline (green), and the ACTV pipeline (blue).

The prototype facilitates collaboration between an External Developer and a Test Service Provider, as shown in Fig. 7. Development and extended pipeline steps occur on the External Developer's side, while ACTV pipeline steps are executed by the Test Service Provider. Docker, a containerization platform, is used to package and distribute applications and dependencies in portable containers, enabling black-box software sharing.

The VP is triggered by a new controller algorithm feature committed to the CI/CD platform. Steps 1.1 to 1.4 involve building code, performing unit tests and static analysis, and generating documentation. Novel validation begins at Step 2, where the External Developer packages software modules as Docker images (Step 2.1) for system validation (Step 3). Validation starts with Step 2.2, where the External Developer runs an ACTV agent (Docker image) provided by the Test Service Provider. The agent interfaces with the test infrastructure, executing system-level validation via ACTV APIs.

The ACTV pipeline begins at Step 3 by retrieving test and simulation specifications from a Git repository, configured by both parties. The Docker images prepared in Step 2.1 are pulled for the next step. Multiple scenarios can be defined using Docker Compose files, dynamically targeted by changing ACTV agent input parameters.

Each controller under test is packed into a Docker container (Step 2.1) and targeted in the Docker Compose file. Docker Compose defines an application stack in a YAML file, managing multiple containers as a single application, suitable for system-level validation.

In Step 3.1, configuration files and test containers are staged. Step 3.2 allocates system resources and real-time simulators for validation. The grid model runs in real-time, deploying the full software stack. Validation progresses to Step 3.3, executing pre-defined tests and recording data. Step 3.4 archives reports and data, transmitting them back to the user as job artifacts accessible via GitLab UI for offline analysis. The External Developer can monitor test progress in real-time through ACTV agent logs (Step 2.2).

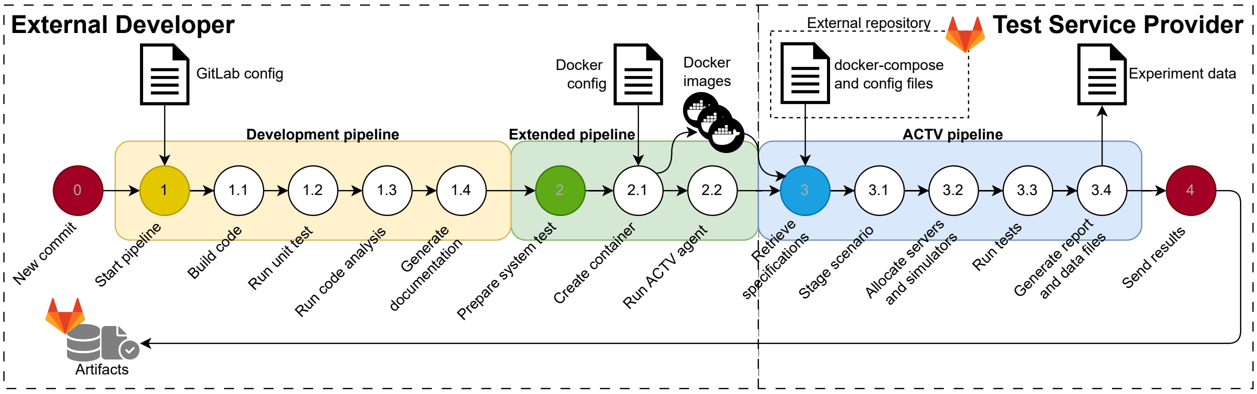

Figure 7: Validation pipeline prototype.

## 4.3 Example Use Case

In this use case, an External Developer wants to validate a smart charging algorithm for electric vehicles (EVs). The Test Service Provider provides tools to test the algorithm.

For the use case, the grid in Figure 8 was used. It represents the residential feeder of the CIGRE European low-voltage distribution network benchmark [37], deployed in a real-time simulator (Opal-RT) using ACTV to validate the EMS. The CIGRE-Network, designed for integrating distributed energy resources (DER), aligns with the SMGW infrastructure and EMS objectives.

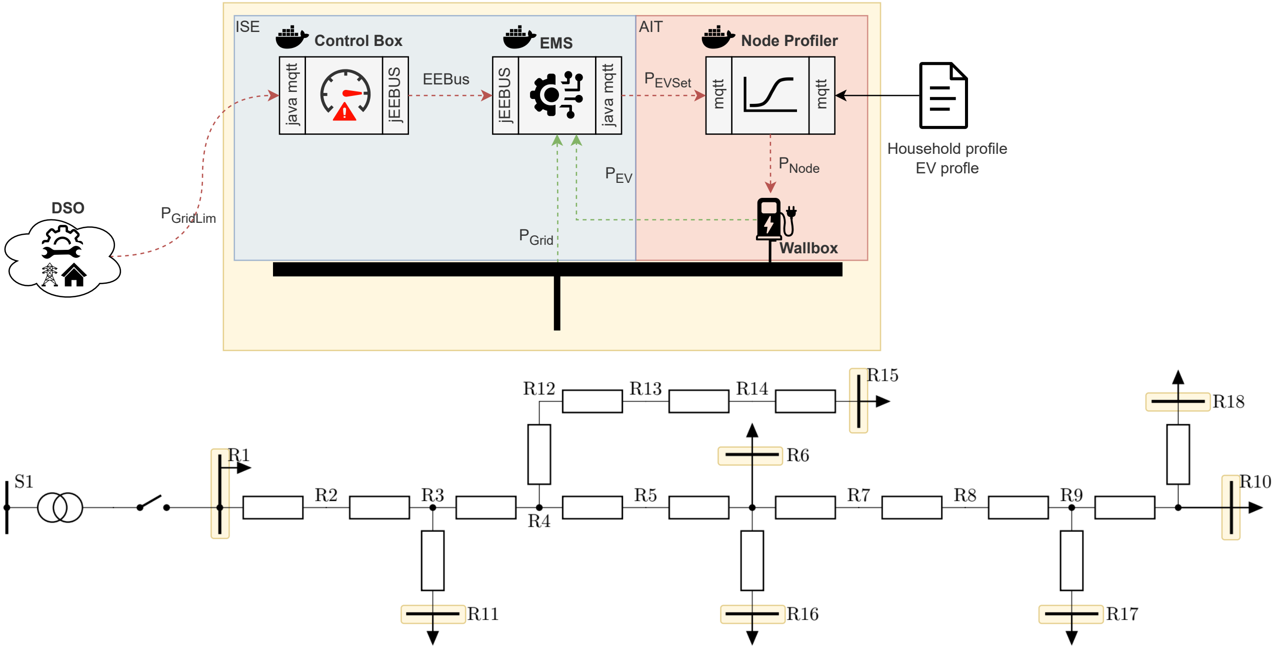

Figure 8: CIGRE network [37] with EMS controllers.

The grid model features eight nodes (yellow in Figure 8), each representing a household with typical loads like appliances and EV charging stations. The Node Profiler (NP) module (red) from AIT applies historical load profiles to the grid and adjusts them based on MQTT topic subscriptions (e.g., PEVSet).

The NP and grid model, stored in the external repository, are essential for validating the Control Box and EMS. The validation process begins with the developer committing a new feature, leading to the creation of Docker images for the Control Box and EMS.

The ACTV stage deploys the grid, NP, Control Box, and EMS images on the Test Service Provider's servers. This automated process allows users to monitor validation pipeline progress via logs. During real-time simulation, the EMS receives grid measurements via MQTT, and the Control Box responds to DSO-imposed consumption limits. The EMS adjusts controllable loads to adhere to these limits, transmitting new setpoints (PEVSet) to the NP, which modifies EV profiles accordingly. All signals exchanged during simulation are recorded.

## 4.4 Test Results

Upon validation pipeline completion, results are presented as artifacts. Figure 9 shows validation outcomes for node R1. The first graph displays the upper boundary of active power (blue) and consumption (red). At 15:06:30 (E1), a new DSO setpoint limits household power to 11kW, and the red line adjusts accordingly. At 15:08:30 (E2), a new 8kW limit is imposed, and EV charging is adjusted.

The second plot in Figure 9 shows historical appliance and EV charging profiles (yellow and green). The green line represents the adjusted EV charging profile post-DSO limitations, demonstrating the EMS's ability to manage consumption within boundaries despite fluctuating appliance loads.

The validation pipeline automates system-level validation of the Control Box and EMS, enabling easy retriggering for new software features.

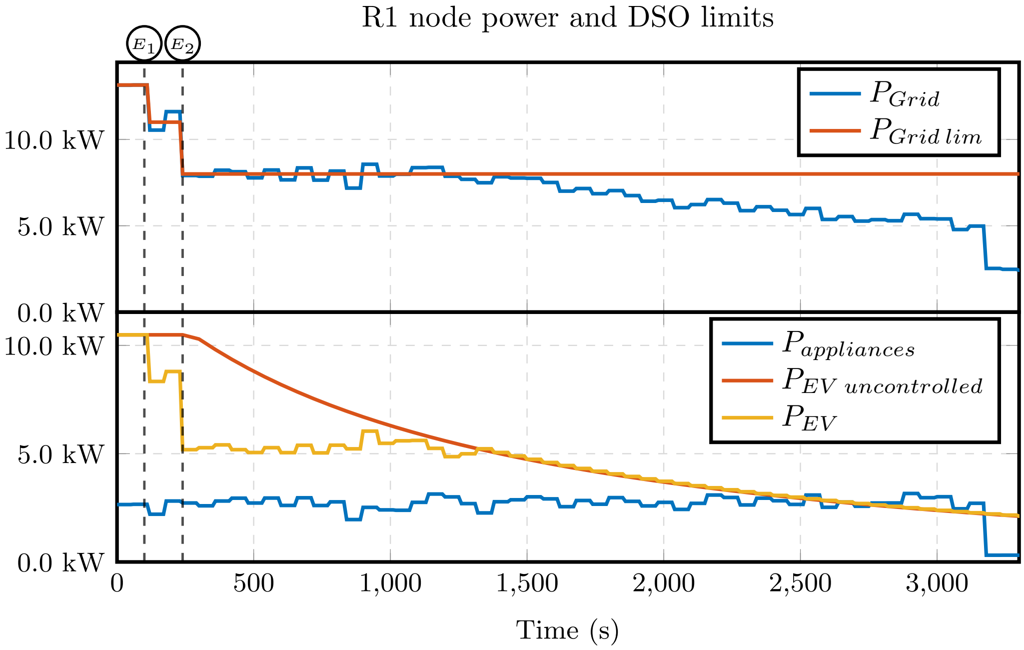

Figure 9: Validation results for node R1.

# 5 Fault Localization in Heterogenous Distribution Grids

Electrical faults and anomalies in high-voltage transmission lines and medium-voltage distribution lines risk interrupting the power supply to large numbers of customers. Line-to-earth fault currents may, for example, result from interactions between power lines and growing tree branches, or from the gradual decay in cable insulation. Often there are early signs of such developing fault conditions, but the resulting earth currents have short duration and are not large enough to trigger the regular protection relays. These fault conditions can, therefore, go unnoticed until they cause a major power outage. However, with access to high-resolution, high-frequency measurements of voltage and current, it is possible to detect and estimate the location of developing faults at an early stage [17]. Such detection systems have many advantages: The line/cable can be repaired before any customer is affected by an outage, and the repair can be scheduled ahead of time, thereby improving system resilience. A reasonable estimate of the distance to the fault can also simplify the repair process since lines can easily span several kilometers. All these factors reduce the cost to both the system operator and the customer.

According to the existing literature, there are four broad classes of methods to estimate fault location: steady-state methods [1, 20], transient-based methods [9, 10], travelling-wave methods [2, 11, 23], and data-driven methods [34, 47]. Helpful overviews are provided in [17, 28]. Many of these rely on measurements from at least two points on the line. In contrast, we will here mainly consider methods that rely on a single measurement point (in a primary substation). Data-driven methods depend on large datasets for training, which may not be available. The steady-state and transient methods are typically based on lumped parameter models.

We consider here an example of a medium-voltage feeder system, which is described in Section 5.1. We present three methods for fault localization: In Section 5.2, we apply the so-called Electro-Magnetic Time Reversal (EMTR) method to the problem and evaluate its performance. The EMTR method belongs to the class of travelling-wave methods. In Section 5.3, we apply what we call the Lumped Parameter Single Feeder (LPSF) method, which is more related to the class of steady-state methods. In Section 5.4, we present a more theoretical approach to the problem based on Partial Differential Equation (PDE) models. Finally, in Section 5.5, we discuss relations between the methods and possibilities for future work.

## 5.1 Example Feeder Model

In this section, we introduce the example feeder used in the fault localization evaluations that follow. It is a rural $11\,\mathrm{kV}$ feeder located in Sweden. DLab has provided the model and data corresponding to voltage and current measurements recorded during actual faults that previously occurred in the network. A detailed simulation model of the feeder was developed for PowerFactory, a power systems simulation tool often used in the field.

A simplified line diagram is shown in Figure 10. In this diagram electrical busses are represented by the nodes of the graph, while the electrical lines connecting the busses correspont to the graph edges. The substation is marked by the green node (bus 10). The feeder has cable (in red) and overhead line (blue) segments. The number on each line segment indicates its length (in $\mathrm{km}$).

In the performed studies, we considered various fault scenarios in 11 different locations along the path leading from bus 20 to bus 82. The distance from the substation to bus 82 is about $4.6\,\mathrm{km}$. During development, additional simulation scenarios were considered for evaluation purposes, including simplifying the topology, removing connecting branches, and converting the feeder to a uniform cable/overhead single-line feeder.

The anomaly/fault scenarios we considered are single-line-to-earth faults at unknown distances from the measurement point. The measurement point is, unless otherwise stated, located in the substation in bus 10. A complication is that the feeder is equipped with a Petersen coil, see, for example,

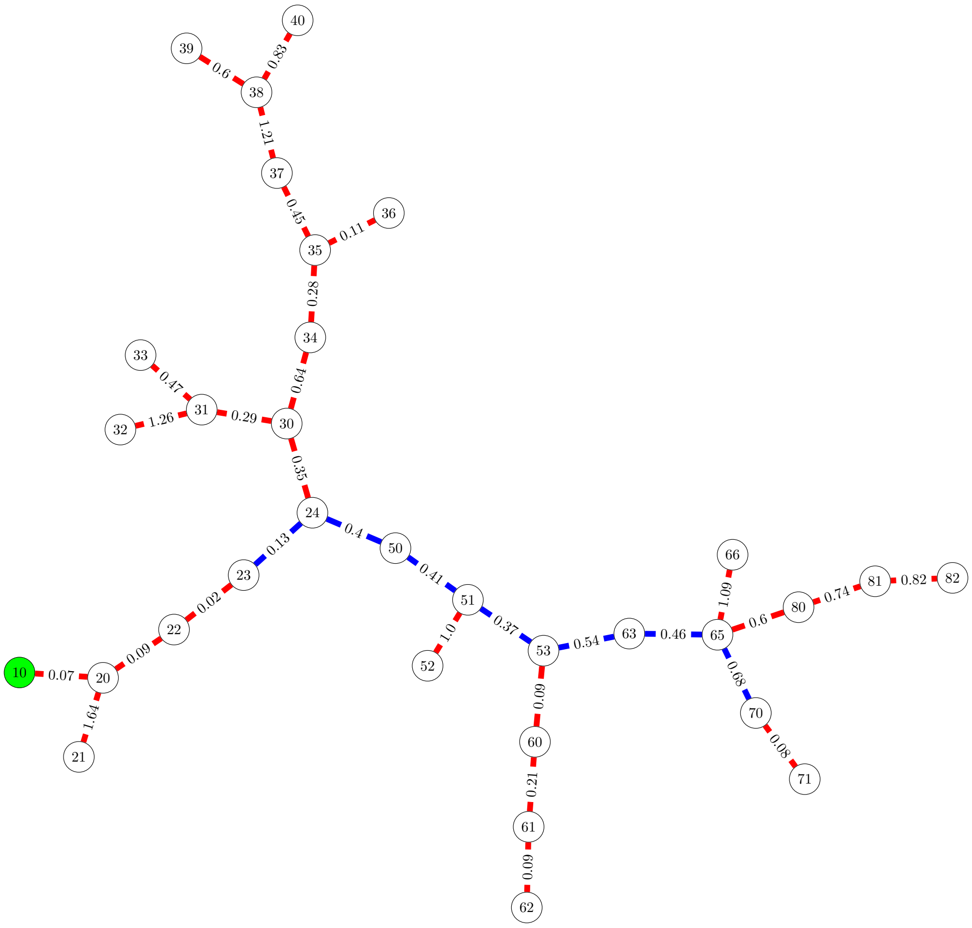

Figure 10: Diagram of the distribution feeder we considered for our study. The substation is in bus 10, and we consider faults in 11 locations on the path leading from bus 20 to bus 82.

[17], tuned to minimize the magnitude and duration of fault currents. This makes the detection and localization of the faults incredibly challenging.

## 5.2 EMTR Method

One of the notable techniques within traveling-wave methods is known as the EMTR method. This approach holds promise in accurately localizing faults and demonstrating high precision and resolution. Initially introduced in [29], subsequent advancements have been made, with a detailed overview available in [41]. However, it needs further validation to assert its effectiveness to locate faults in complex distribution networks.

We validated its performance considering the single feeder network in Figure 10. Validation shows that the method is able to accurately localise faults. However, a single measurement point may not be sufficient to locate faults throughout the network. A possible explanation is given, and the use of a second sensor is proposed to extend the performance of the method.

### 5.2.1 Method description

The EMTR method has originally been formalized as follows. The fault localization process can be delineated into two main phases. In the initial phase, termed the forward propagation stage, the voltage and/or current transients resulting from a fault event are captured at one or more measurement points distributed throughout the network [41]. Following this, in the second phase, known as the backward propagation stage, the recorded signals are time-reversed and numerically reintroduced into a detailed model of the network. This simulation can be executed using either time-domain simulation tools [42] or in the frequency domain [19]. Subsequently, upon identifying a set of potential fault locations, individual simulations are conducted for each candidate location, where the fault is linked to the respective spot. Operating under the assumption that optimal focusing occurs when the backward-propagation medium aligns with the forward-propagation medium, i.e., when the fault is located at the actual fault position, the fault's precise location is determined by maximizing a predefined metric that quantifies the focusing effect among the chosen candidates.

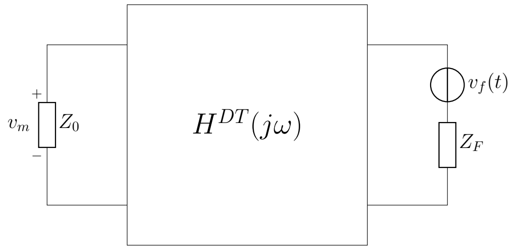

Figure 11: Forward propagation

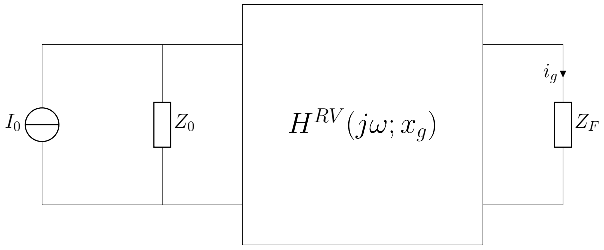

Figure 12: Backward propagation

In Figure 11 and Figure 12 the two phases are depicted, where $v_f$ is the fault voltage, $Z_f$ the fault impedance, $Z_0$ the sensor impedance, $v_m$ the measured voltage, and $H^{DT}(j\omega; x_f)$ is the transfer function from $v_f$ to $v_m$, which depends on the location of the fault $x_f$. In the backward propagation diagram, the recorded signal $v_m$ is re-injected into the network model using the Norton equivalent composed by $I_0 = v_m(-t)/Z_0$ and $Z_0$. $H^{RV}(j\omega; x_g)$ is the transfer function from $I_0$ to $i_g$, the fault current, which depends on the guessed fault location $x_g$. In [4], considering a single transmission line, it is proved that $H^{DT}(j\omega; x_f) = H^{RV}(j\omega; x_g)$ if and only if $x_f = x_g$. It is reasonable to expect that this condition holds also for more complex networks, and it is validated later.

The metric proposed in [29] is the fault current energy that reads as follows:

$$||i_g(t; x_g)||_2 = \int |i_g(t; x_g)|^2 dt \tag{1}$$

or in frequency domain as[2]:

$$||i_g(t; x_g)||_2 = \int |V_m^*(j\omega) H^{RV}(j\omega; x_g)|^2 d\omega \tag{2}$$

Finally, the fault location is estimated as

$$\hat{x}_g = \arg\max_{x_g} ||i_g(t; x_g)||_2 \tag{3}$$

The frequency form of the fault current energy in (2) gives a spectral interpretation why this metric is a proper metric to determine the fault location. In fact, the metric can be seen as the covariance between the squared magnitude of the recorded signal $V_m(j\omega)$ and the transfer function $H^{RV}(j\omega; x_g)$. Therefore, the metric is used to compare the spectrum of the recorded voltage with the spectrum of different fault location dependent models, and the fault location is selected as the one with higher spectrum similarity.

The calculation of the metric can be performed in the time domain as in (1) or in frequency domain as in (2). While in the time domain, for each guessed fault location a simulation has to be performed re-injecting the fault transient and recording the resulting fault current $i_g$, in the frequency domain the impulse response $H^{RT}$ for each fault is precomputed numerically, stored and used to compute the metric, as shown in (2). In case a large number of fault location needs to be tested, the frequency domain is preferable since all the impulse responses can be pre-computed and the computation of the metric is much faster than running all the simulations in the time domain. For this reason, the frequency domain metric was adopted for this study.

---

[2] Here $Z_0$ is ignored since it does not depends on $x_g$

### 5.2.2 Method implementation and validation

The method is tested on the network shown in Figure 10. A model of the network under test has been developed in DIgSILENT PowerFactory simulation software. Although not shown, loads are connected to some buses of the network, through transformers. Since the method uses the high frequency line dynamics to identify the fault location, the distributed parameter line model is adopted. To correctly simulate the model, a small integration time needs to be chosen. This depends on the shorter line propagation delay. In our case, it has been chosen to be $100\mathrm{ns}$.

The fault transient sensor is placed at the substation at bus $10$.

To validate the method, we consider a fault for each bus in the network and validate the capability of the method to correctly identify that bus as the fault location, considering all the buses as possible fault locations. Only single-phase to ground faults are considered in this study since it is the most common fault type. The fault is assumed to be purely resistive with resistance equal to $0.1\Omega$, therefore considering an almost solid fault.

For each possible fault location, the respective transfer function $H^{RV}$ is computed. To do so, the impulse response from the input variable $I_0$ to the output variable $i_g$ is simulated numerically. Then, the transfer function is obtained by applying the FFT to the resulting signal. Since we are working with a three-phase system, for each phase the transfer function is computed and the metric in (2) is modified as

$$||i_g(t;x_g)||_2 = \int_{\mathcal{B}} \left| \sum_{ph=a,b,c} V^*_{ph,m}(j\omega) H^{RV}_{ph}(j\omega;x_g) \right|^2 d\omega \tag{4}$$

where the fact that the integral is computed over the frequency band $\mathcal{B}$ is also emphasize.

### 5.2.3 Network spectral analysis

Before proceeding with the validation, a spectrum analysis is performed. First, we validate the assumption $H^{DT}(j\omega;x_f) = H^{RV}(j\omega;x_g)$ if and only if $x_f = x_g$ still holds for complex networks. In Figure 13 the backward transfer function at bus $37$, i.e. $H^{RV}_{37}$, is compared with the respective forward transfer function $H^{DT}_{37}$ and the transfer functions of the two closest buses $35$ and $38$. As one can check, the transfer functions match perfectly only when the same fault location is assumed in the forward and backward transfer function, validating the mentioned assumption.

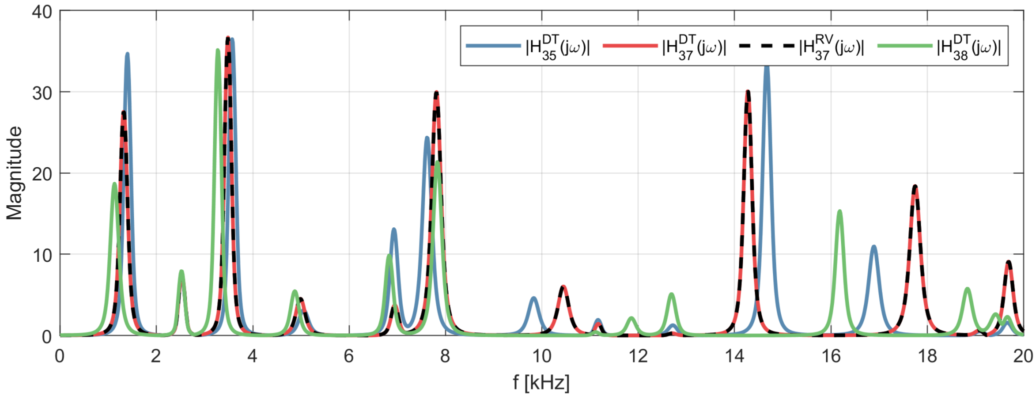

Figure 13: Spectrum of forward and backward transfer functions

Secondly, we compare the spectrum of the generated fault transient, see Figure 14, to check which frequency band to take into consideration when computing the location metric. As one can notice, each fault generates a unique signature in the spectrum, and this aspect is the underlying fundamental behind the EMTR method. In the low frequency band, below $3$ kHz, the resonance peaks are very close each other, therefore it is preferable to exclude this band from the metric (4) since it can give rise to wrong fault location estimation. Given that the sensor bandwidth must be as low as possible to reduce the costs of the sensor device, the metric (4) is calculated considering the frequency band $\mathcal{B} = [3, 20]$ kHz.

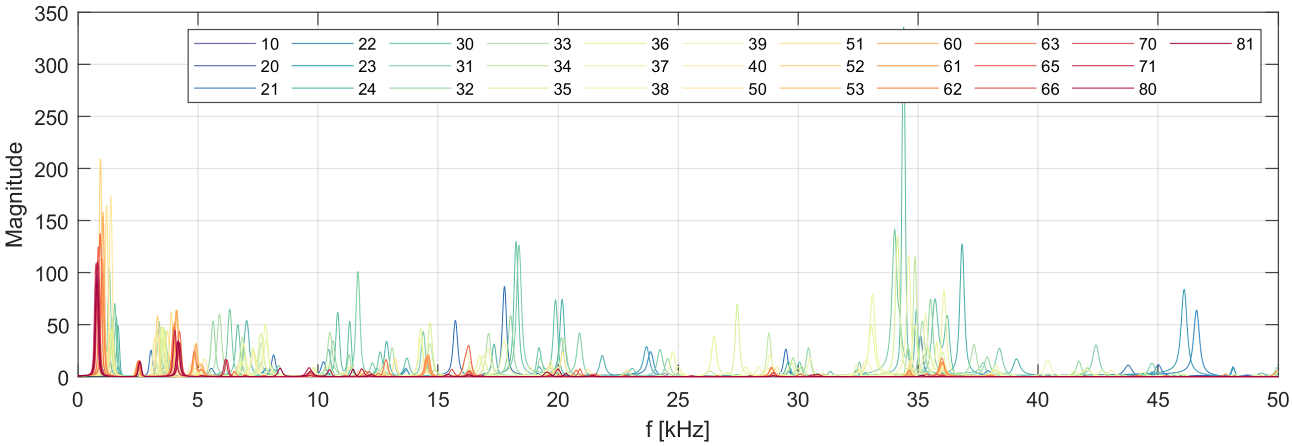

Figure 14: Fault spectrum for different fault locations

### 5.2.4 Results

In Figure 15a the results of the EMTR method applied to the network under test are shown. For each bus fault on the vertical axis, the metric in (4), normalized with respect to the maximum value, is shown in the respective row. If the maximum value, i.e. one, is reached on the same bus of the fault, the algorithm identifies the fault location correctly, otherwise it does not.

As it can be seen, for buses numbered from 10 to 52, the matrix is diagonal dominant, which implies high estimation accuracy. However, for buses 53 to 81, the algorithm is unable to accurately determine the correct fault location. This aspect has been further analyzed and the reason for this lies in the network topology and the use of different types of lines, cabled and overhead lines, which present different propagation characteristics.

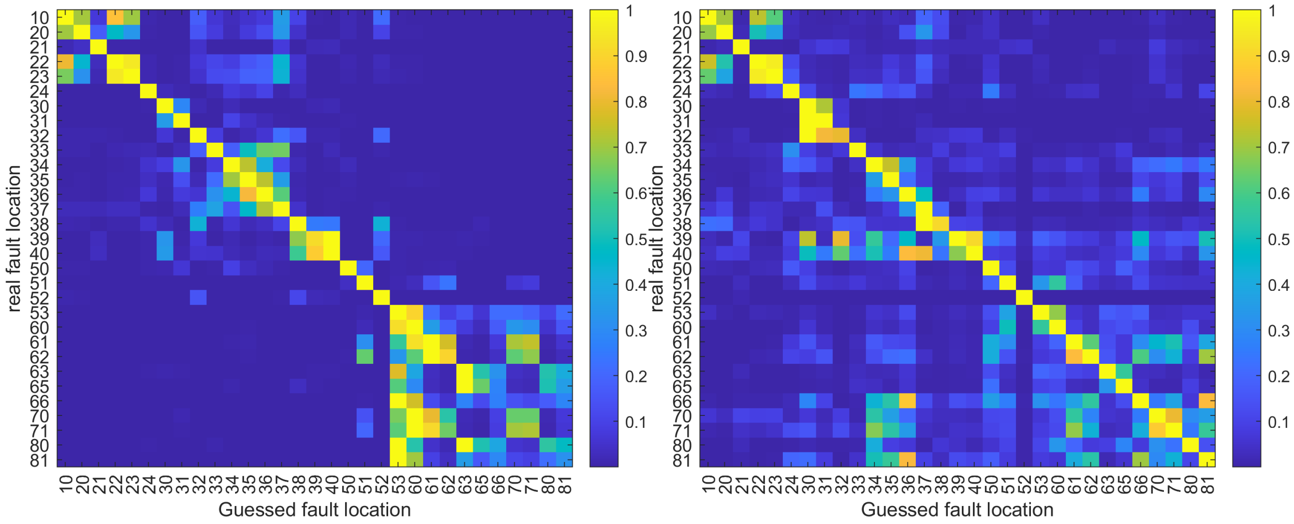

(a) Original network

(b) Overhead lines replaced by cables

Figure 15: Fault location validation for sensor $10$

## 5.3 LPSF Method

As an alternative to the EMTR method for fault localization, we will investigate a method developed in the PhD thesis [16]. The method is based on a simplified lumped-parameter model of a single feeder and is denoted the LPSF method[3] in the following. Based on steady-state phasor measurements of currents and voltages at the substation and assuming the faulty branch is known, the distance for the fault is estimated. The method is described in some detail in the following. In comparison to EMTR, the LPSF does not require repeated simulation of a complete network model and is, in this sense, more "lightweight." On the other hand, the LPSF method requires a numerical solution to an optimization problem, which generally is non-convex. Furthermore, the theoretical justification and understanding of the LPSF method are less developed.

In this section, we evaluate three versions of the LPSF method on the example feeder in Section 5.1, both in a simulated and a real scenario.

### 5.3.1 Method Description

The method in [16] assumes that the fault occurs at a relative distance $x$, $0 \leq x \leq 1$, from the measurement point (the primary substation) in a single feeder, as is illustrated in Figure 16. The modeling assumes steady-state conditions before and after the fault occurs and decomposes the three-phase model using standard symmetrical components [15]. Here, we denote the positive sequence by subscript $1$, the negative sequence by subscript $2$, and the zero sequence by subscript $0$. The model is relatively standard, except for the shunt elements in the zero sequence, which account for capacitive coupling to earth ($Y_0$) and neighboring feeders ($Y_{0\text{bg}}$), as well as Petersen coil impedance ($Z_{\text{PC}}$) and resistance ($R_{\text{P}}$). Figure 16 displays the situation before the fault, and Figure 17 during a single-phase to earth fault (assuming a steady state has had time to be established).

**Remark 5.1** *Note that the model in Figure 17 assumes that all loads are allocated* after *the fault location. This will not always be the case in the investigated fault scenarios for our example feeder in Section 5.1. Part of the evaluation here is to clarify the importance of this assumption.*

Next, we will present three variations of the LPSF method.

**Fault Current Measurement (OPT1).** The fault current $I_{\text{F}}$ in Figure 17 is generally not measurable since the fault location is unknown. In this first instantiation of the LPSF method, *we assume it is available*, however. The main reason for making this assumption is that it provides insights on the "best possible" fault distance estimates using a simple LPSF model.

The estimated distance $x$ of the fault is obtained by solving the optimization problem

$$\begin{aligned} \text{minimize} \quad & \left| V_{\text{ph}} - x(Z_0 I_0 + Z_1 I_1 + Z_2 I_2) + x^2 \frac{Y_0 Z_0}{2} V_0 - 3 R_{\text{F}} I_{\text{F}} \right| \\ \text{subject to} \quad & 0 \leq x \leq 1, \\ & 0 \leq R_{\text{F}}, \end{aligned} \tag{OPT1}$$

with variables $x$, $R_{\text{F}} \in \mathbb{R}$, and fault recording $V_{\text{ph}} := V_0 + V_1 + V_2$, $I_0$, $I_1$, $I_2 \in \mathbb{C}$, *and* $I_{\text{F}} \in \mathbb{C}$. Note the fault current $I_{\text{F}}$ is here the sequence-component value ($1/3$ of the value of the fault current itself), and that the fault resistance $R_{\text{F}}$ is assumed unknown and is estimated by the method.

**Remark 5.2** *To solve* (OPT1) *(and* (OPT1') *and* (OPT2) *in the following), we have used a Sequential Least Squares Programming (SLSQP) method in the Python function* `scipy.optimize.minimize`. *To initialize the iterative optimization method, we use* $(x, R_{\text{F}}) = (0, 0)$.

---

[3] Our terminology.

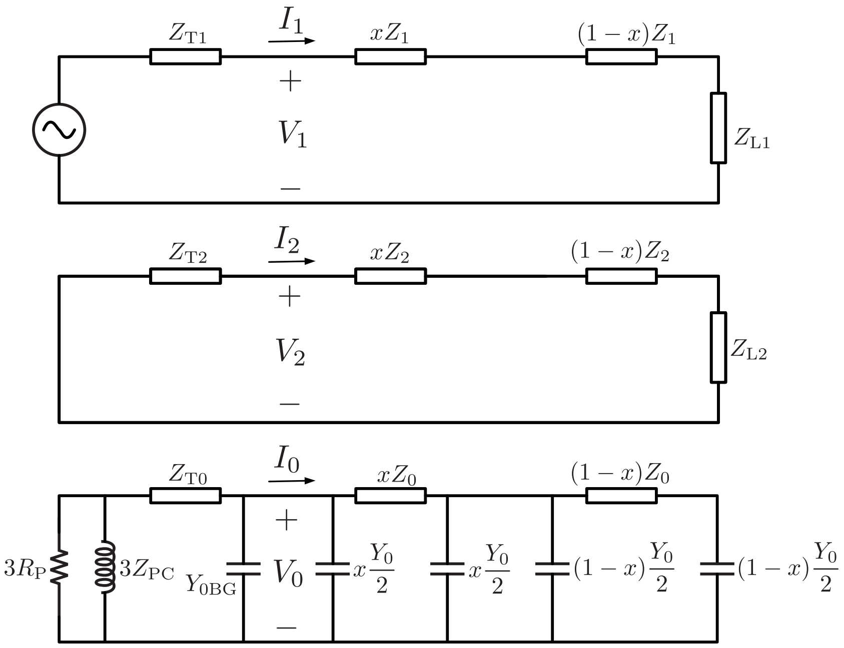

Figure 16: Sequence diagram of the LPSF model (pre fault). Adapted from [16, Chapter 4].

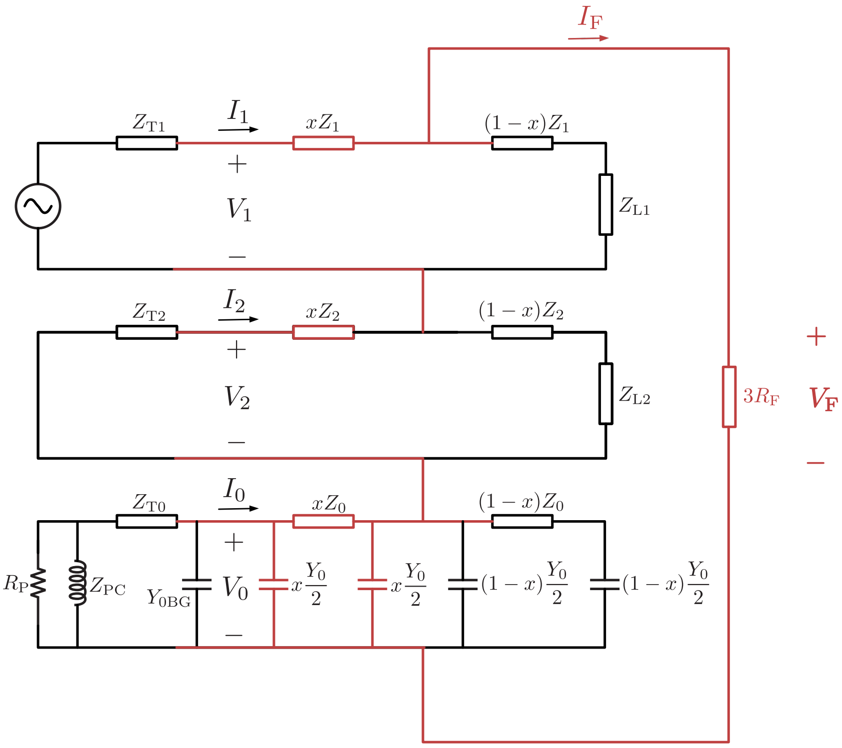

Figure 17: Sequence diagram of the LPSF model (during fault). Adapted from [16, Chapter 4].

**Model-based Fault Current Estimate (OPT1').** Using the method in [16], the estimated distance $x$ of the fault is computed by solving the optimization problem

$$\begin{array}{ll} \text{minimize} & \left| V_{\mathsf{ph}} - x(Z_0 I_0 + Z_1 I_1 + Z_2 I_2) + x^2 \dfrac{Y_0 Z_0}{2} V_0 - 3R_{\mathsf{F}} \hat{I}_{\mathsf{F}} \right| \\ \text{subject to} & 0 \leq x \leq 1, \\ & 0 \leq R_{\mathsf{F}}, \end{array} \tag{OPT1'}$$

with variables $x$, $R_\mathsf{F} \in \mathbb{R}$, and fault recording $V_\mathsf{ph} := V_0 + V_1 + V_2$, $I_0$, $I_1$, $I_2 \in \mathbb{C}$, and the following model-based estimate of the fault current [16]

$$\hat{I}_\mathsf{F} = \left( \frac{1}{3R_\mathsf{P}} + \frac{1}{3Z_\mathsf{PC}} + Y_0 + Y_{0\mathsf{BG}} \right) V_0 \in \mathbb{C}. \tag{5}$$

Notably, this method does not require measurement of the fault current. Instead, model parameters of capacitive coupling and the Petersen coil are required in (5). Regarding (5), Habib [16, Chapter 4] remarks, “However, the proposed solution is sensitive to fault resistances and requires good knowledge of zero sequence parameters.” Thus the comparison with (OPT1) is of interest.

**Data-based Fault Current Estimate (OPT2).** The method (OPT1’) requires a detailed model of the zero sequence model parameters. Our final version (OPT2) attempts to circumvent this (potential) sensitivity by exploiting data from recurrent but independent faults at the same location $x$. We assume that $N > 1$ recurrent faults have been recorded and that we have obtained voltage and current phasor measurements at the substation, as before. A quantity from fault $i$ has superscript $(i)$ next. The measurements will be stacked into an $N$-dimensional vector $\mathbb{C}^N$, and the model misfit is evaluated using a $p$-norm, $\| \cdot \|_p$, with

$$p \in \{1, 2, \infty\}.$$

Instead of using (5), we here make the *assumption*

$$I_\mathsf{F}^{(i)} \approx T_\mathsf{F} I_0^{(i)}, \quad T_\mathsf{F} = |T_\mathsf{F}| e^{j\phi} \in \mathbb{C}, \quad |\phi| \leq \pi/2, \tag{6}$$

for $i = 1, 2, \ldots, N$. That is, for all fault scenarios at location $x$, a constant complex ratio $T_\mathsf{F}$ of the measured zero sequence current $I_0$ is related to the fault current $I_\mathsf{F}$. For the method to work, it is assumed that each fault scenario has a sufficiently different fault resistance $R_\mathsf{F}^{(i)}$, such that the new optimization variables $K^{(i)} := R_\mathsf{F}^{(i)} |T_F| \in \mathbb{R}$ can be determined.

**Remark 5.3** *The constraint* $|\phi| \leq \pi/2$ *in* (6) *ensures that the fault current and zero sequence current are somewhat in phase, which seems reasonable from the sequence diagram. However, this constraint is not critical and can easily be relaxed to another bound in* (OPT2)*.*

The estimated distance $x$ is computed by solving

$$\begin{array}{ll} \text{minimize} & \left\| \begin{bmatrix} V_\mathsf{ph}^{(1)} - x(Z_0 I_0^{(1)} + Z_1 I_1^{(1)} + Z_2 I_2^{(1)}) + x^2 \frac{Y_0 Z_0}{2} V_0^{(1)} - 3K^{(1)} e^{j\phi} I_0^{(1)} \\ V_\mathsf{ph}^{(2)} - x(Z_0 I_0^{(2)} + Z_1 I_1^{(2)} + Z_2 I_2^{(2)}) + x^2 \frac{Y_0 Z_0}{2} V_0^{(2)} - 3K^{(2)} e^{j\phi} I_0^{(2)} \\ \vdots \\ V_\mathsf{ph}^{(N)} - x(Z_0 I_0^{(N)} + Z_1 I_1^{(N)} + Z_2 I_2^{(N)}) + x^2 \frac{Y_0 Z_0}{2} V_0^{(N)} - 3K^{(N)} e^{j\phi} I_0^{(N)} \end{bmatrix} \right\|_p \\ \text{subject to} & 0 \leq x \leq 1, \\ & -\pi/2 \leq \phi \leq \pi/2 \\ & 0 \leq K^{(i)}, \; i = 1, 2, \ldots, N, \end{array} \tag{OPT2}$$

with variables $x$, $\phi$, $K^{(i)} \in \mathbb{R}$, and fault recordings $V_\mathsf{ph}^{(i)} := V_0^{(i)} + V_1^{(i)} + V_2^{(i)}$, $I_0^{(i)}$, $I_1^{(i)}$, $I_2^{(i)} \in \mathbb{C}$.

### 5.3.2 Simulation Results (OPT1)

In this test, we evaluate (OPT1) on the feeder shown in Figure 10. More detailed simulations results can be found in [31]. As mentioned, (OPT1) assumes the fault current is known, and as such, the results here provide insight into the best possible results from the LPSF method.

The feeder in Figure 10 has a mixture of overhead line and cable sections. In contrast, the LPSF method assumes a uniform line impedance[4]. To further check the accuracy, we first, in simulation, use cable sections and disconnect all branches to come as close as possible to the LPSF model. We then simulate faults with $R_\mathsf{F} = 50\,\Omega$ in $11$ locations gradually moving away from the substation. The obtained location estimates $x$, together with the actual distances, are shown in Figure 18. As can be seen, the estimates are very accurate and verify that the method under idealized conditions performs very well.

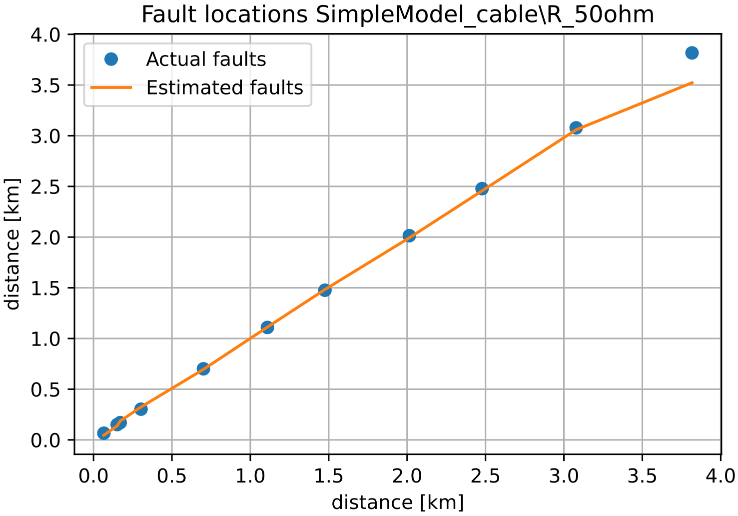

Figure 18: Solution to (OPT1) assuming a uniform cable model, all load branches disconnected, and $R_\mathsf{F} = 50\,\Omega$.

In Figure 19, we perform similar tests with the actual overhead line and cable sections and load branches along the feeder for four fault scenarios. Notice that this feeder is much more complex than what is assumed in Figure 17, and it is by no means clear how well, or if, (OPT1) will work. The scenarios with $R_\mathsf{F} = 3000\,\Omega$ and $5000\,\Omega$ are high-ohmic faults resulting in tiny fault currents and are expected to be especially challenging. For the low-ohmic faults $R_\mathsf{F} = 10\,\Omega$ and $50\,\Omega$, the location estimates are not as accurate as in Figure 18, but up to around $2\,\mathrm{km}$ are still very good for the low-ohmic faults. Also, beyond $2\,\mathrm{km}$, the low-ohmic estimates could be of value in practical fault localization scenarios.

In the challenging high-ohmic cases, the estimates start to diverge after around $1\,\mathrm{km}$. It is also interesting to notice that the estimates are almost identical for $R_\mathsf{F} = 3000\,\Omega$ and $5000\,\Omega$.

### 5.3.3 Experimental Results (OPT1') and (OPT2)

DLab provided fault recordings from an actual fault on the feeder in Figure 10. Two different recordings, Scenario 14777 and 14783 from the same location $x = 2.478\,\mathrm{km}$ are available. For reference, the length of the feeder is $4.635\,\mathrm{km}$. Scenario 14777 was recorded by the dLab system in the actual feeder on August 20, 2022, at 06:41:48. The fault was classified as “Dense earth fault transients that evolves into short circuit.” The Scenario 14783 was recorded on the same date, at 09:01:38 (about 2 hours and 20 minutes later), as was classified as “Energizing a faulted line, faulty surge arrestor.” Since the true fault current is not measured, only (OPT1') and (OPT2) are applicable here. The results are in Table 1.

Notably, (OPT1') provides a reasonable location estimate in Scenario 14783. However, the result for Scenario 14777 is far beyond the actual fault location, just as in the simulation study. Again, this illustrates the sensitivity of the fault estimate (5).

---

[4] It is possible to take non-uniform line segments into account by introducing piece-wise linear (in $x$) line impedances. We leave this for future work.

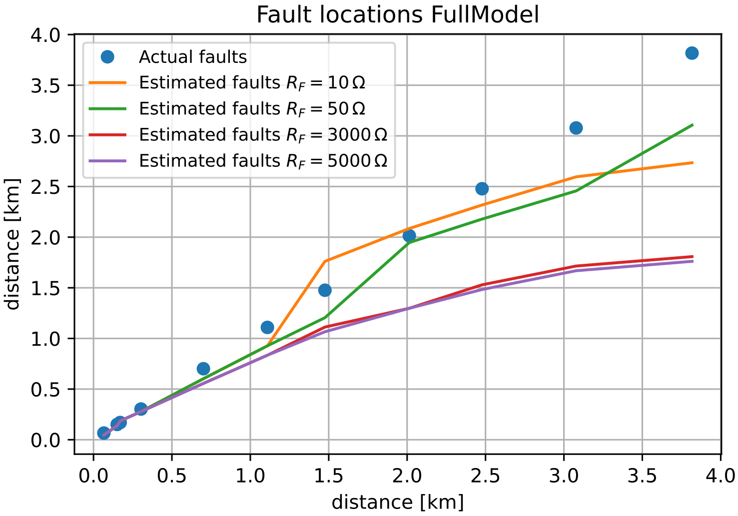

Figure 19: Solution to (OPT1) assuming the full feeder model, with a mixture of cable and overhead line sections, load branches connected, and $R_\mathrm{F} = 10\,\Omega$, $50\,\Omega$, $3000\,\Omega$, and $5000\,\Omega$.

The method (OPT2) provides an estimate using both scenarios ($N = 2$). The estimate does not depend significantly on the choice of $p$-norm, and has a relative accuracy of around $11\,\%$. This is encouraging, but further investigations are suggested.

Table 1: Results from experimental data.

| Scenario | Method | True $x$ | Estimated $x$ | Relative Error |
|---|---|---|---|---|
| 14777 | (OPT1') | $2.478\,\mathrm{km}$ | $4.635\,\mathrm{km}$ | $87.0\,\%$ |
| 14783 | (OPT1') | $2.478\,\mathrm{km}$ | $2.874\,\mathrm{km}$ | $16.0\,\%$ |
| 14777+14783 | (OPT2), $p = 1$ | $2.478\,\mathrm{km}$ | $2.749\,\mathrm{km}$ | $11.0\,\%$ |
| 14777+14783 | (OPT2), $p = 2$ | $2.478\,\mathrm{km}$ | $2.749\,\mathrm{km}$ | $10.9\,\%$ |
| 14777+14783 | (OPT2), $p = \infty$ | $2.478\,\mathrm{km}$ | $2.749\,\mathrm{km}$ | $10.9\,\%$ |

### 5.4 PDE-Method

This method focuses on estimating the fault distance along a single transmission line, resulting in a parameter estimation problem for an infinite-dimensional linear dynamical system with one spatial variable.This problem pertains to estimating the fault distance along a single branch in Figure 10, once the identity of the branch has been determined by other methods. A frequency-domain least-squares approach is adopted. Since the time of the fault is unknown, and voltages and currents are measured at only one end of the line, distance information must be extracted from the post-fault transients. To properly account for high-frequency transient behaviour, the line dynamics are modelled directly by the Telegrapher's equation, rather than the more commonly used lumped-parameter approximations. A closed-form expression for the transfer function is first derived. Then, nonlinear least-squares optimisation is employed to search for the fault location. Requirements on fault bandwidth, sensor bandwidth and simulation time-step are also presented. The following sections provides an overview of the method and simulation results. More details have been published in [33].

### 5.4.1 Modelling

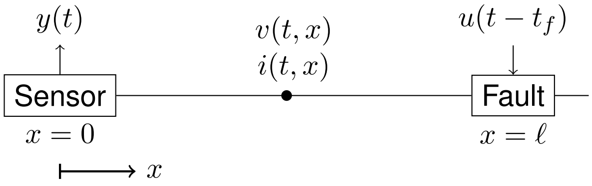

Figure 20: Distribution line diagram

Consider Figure 20. Let $v(t,x)$ denote the voltage at time $t \geq 0$ and position $x \geq 0$ along an electrical distribution line, and $i(t,x)$ the corresponding current. Sensors measure the voltage and current at position $x = 0$. Suppose a fault occurs at position $\ell > 0$ along the line. Restricting attention to the segment of the line between fault and sensors, we assume both $v : [0,\infty) \times [0,\ell] \to \mathbb{R}$ and $i : [0,\infty) \times [0,\ell] \to \mathbb{R}$ are continuously differentiable maps. The spatio-temporal relationship between current and voltage is then modelled by the Telegrapher's equation

$$\begin{bmatrix} C & 0 \\ 0 & L \end{bmatrix}\begin{bmatrix}\frac{\partial v}{\partial t}\\ \frac{\partial i}{\partial t}\end{bmatrix} = \begin{bmatrix}0 & -1\\ -1 & 0\end{bmatrix}\begin{bmatrix}\frac{\partial v}{\partial x}\\ \frac{\partial i}{\partial x}\end{bmatrix} - \begin{bmatrix}G & 0\\ 0 & R\end{bmatrix}\begin{bmatrix}v\\ i\end{bmatrix}, \tag{7}$$

where $R, L, C, G \geq 0$ are constants denoting, respectively, the distributed line resistance, inductance, capacitance, and conductance, per unit length. We assume, in particular, that $R, L, C > 0$. The goal is to estimate the fault location $\ell$ from the sensor measurements $v(t,0)$ and $i(t,0)$.

### 5.4.2 Numerical Case Study

We now tackle a particular instance of the fault localization problem involving a 220kV distribution line in the Swedish power grid. The line parameter values in Table 2 are derived from [38, Table 4], after conversion into SI units. We now simulate the fault in Table 2, and estimate its location using the proposed least-squares procedure. This example serves as a case study to illustrate the main steps involved, highlight important issues, and develop guidelines for both design and simulation.

Table 2: Parameter values for fault localisation case study

| Parameter | Symbol | Value | Units |
|---|---|---|---|
| Line resistance | $R$ | $5.3900 \times 10^{-5}$ | $\Omega\,\mathrm{m}^{-1}$ |
| Line inductance | $L$ | $1.3114 \times 10^{-6}$ | $\mathrm{H}\,\mathrm{m}^{-1}$ |
| Line capacitance | $C$ | $9.1001 \times 10^{-12}$ | $\mathrm{F}\,\mathrm{m}^{-1}$ |
| Line admittance | $G$ | $0$ | $\mathrm{S}\,\mathrm{m}^{-1}$ |
| Base voltage | $V_0$ | $220 \times 10^{3}$ | $\mathrm{V}$ |
| Base current | $I_0$ | $454.55$ | $\mathrm{A}$ |
| Fault resistance | $r$ | $5$ | $\Omega$ |
| Fault time | $t_f$ | $0.01$ | $\mathrm{s}$ |
| Fault distance | $\ell$ | $2000$ | $\mathrm{m}$ |

### 5.4.3 Bandwidth considerations

Figure 21 plots the magnitude spectrum of the transfer function $H$ for the given problem data, at different values of $\ell$. It illustrates a general pattern that can be empirically observed:

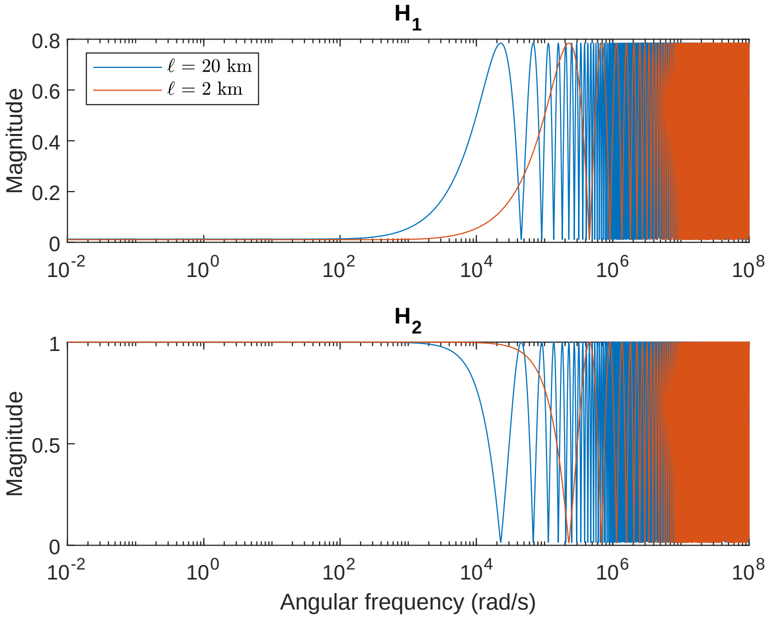

Figure 21: Magnitude spectrum of $H(s;\ell)$, given data in Table 2, for different fault distance values.

- For each value of $\ell$, the frequency response of both components are flat until a critical frequency $\omega^\star$, at which they begin to change.
- The DC gains $h_1 := |H_1(0;\ell)|, h_2 := |H_2(0;\ell)|$ are approximately constant with $\ell$.
- The critical frequency $\omega^\star$ decreases with $\ell$.

Such behaviour has important practical ramifications for modelling, sensing, and simulation.

### 5.4.4 Fault modelling

Our proposed estimation scheme relies on an assumed fault profile $u$. The ideal fault (from a localisation perspective) is an impulse, because it excites all frequencies equally. This is also consistent with the sudden and fleeting nature of line-to-earth faults. However, the finite sensor bandwidth $\omega_b$ implies that all information beyond this frequency is lost. In simulation, numerical PDE solvers must resort to finite time-steps, so they are also unable to reproduce dynamics beyond a certain frequency. For simulation purposes, we therefore model the fault as a Gaussian pulse

$$u(t) = \frac{1}{\sigma\sqrt{2\pi}} e^{-\frac{t^2}{2\sigma^2}},$$

which approaches the unit impulse as $\sigma \to 0$. Its Fourier Transform is a Gaussian pulse in the frequency domain,

$$U(j\omega) = e^{-\frac{\omega^2\sigma^2}{2}},$$

which is clearly bandlimited. Referring to Figure 21, the critical frequency for a fault at $\ell = 2$ km is $\omega^\star \approx 10^4$ rad/s. We choose $\sigma = 3.0349 \times 10^{-5}$ s to obtain a fault bandwidth of $\omega_f = 10^5 \text{ rad/s} > \omega^\star$. The fault spectrum is plotted in Figure 22.

**Remark 5.4** *A Gaussian fault profile is chosen here as an example of a bandlimited pulse, because PDE solvers and physical sensors cannot reproduce arbitrarily high frequencies. In reality, it is difficult* *to know the true current and voltage signals at the fault location, because sensors are never present exactly where a fault occurs. Different types of faults are possible [14, Chapters 8 & 10], and they are expected to produce different profiles. Future work will explore the use of unknown input observers [3, 13] to deal with uncertainty in the fault profile. In a nominally balanced 3-phase system, it may even be possible to estimate the fault current profile from the symmetrical zero sequence component.*

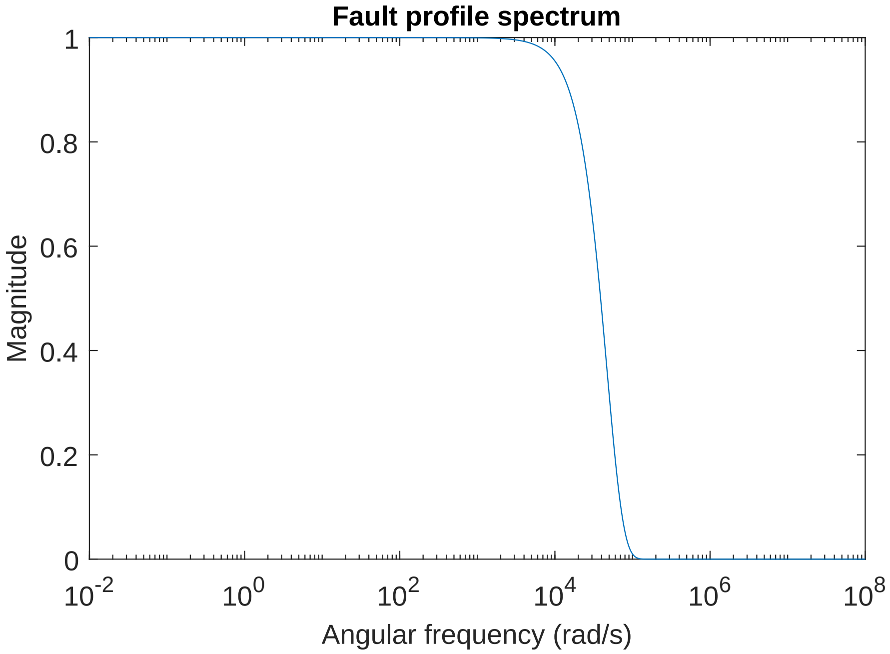

Figure 22: Magnitude spectrum of fault profile, for $\sigma = 3 \times 10^{-3}$.

### 5.4.5 Simulation of PDE dynamics

A fixed simulation time-step of $T_s > 0$ effectively models a sensor with the same sampling period, which corresponds to a sensor bandwidth $\omega_b = \frac{\pi}{T_s}$ equal to the Nyquist frequency. In order to faithfully simulate the line dynamics over the frequency range $[\omega^\star, \omega_f]$, we must have $\omega_b \gg \omega_f$. For this case study, let $T_s = \frac{\pi}{10\omega_f}$, which corresponds to $\omega_b = 10\omega_f$. To simulate the line dynamics, we have used the PIETOOLS [36] numerical PDE solver, which employs Petrov-Galerkin projection onto a polynomial basis, together with the backward-difference discretisation of temporal derivatives. The simulated sensor outputs are plotted in Figure 23. The non-dimensionalisation is necessary for backward-difference to be numerically stable under this choice of time-step and parameter values, but it may not remain so for arbitrarily small time-steps. If numerical instability is encountered for the chosen time-step, other integration schemes may be required. In particular, [8,21,26,30,35] propose numerical methods that are specialised for the Telegrapher's equation. For a real-world localisation problem, the voltage and current initial conditions would reflect the steady-state solution of the power line in response to sinusoidal forcing. However, due to linearity, the corresponding frequency component can simply be removed from the output spectrum before performing the minimisation. This step has been omitted for simplicity. Instead, the line has been simulated with zero initial conditions.

### 5.4.6 Estimation

To illustrate the effect of fault bandwidth and simulation time-step on estimation quality, Figure 24 plots the cost function for different values of $\omega_f$ and $\omega_b = \frac{\pi}{T_s}$. For the blue line, the guidelines are

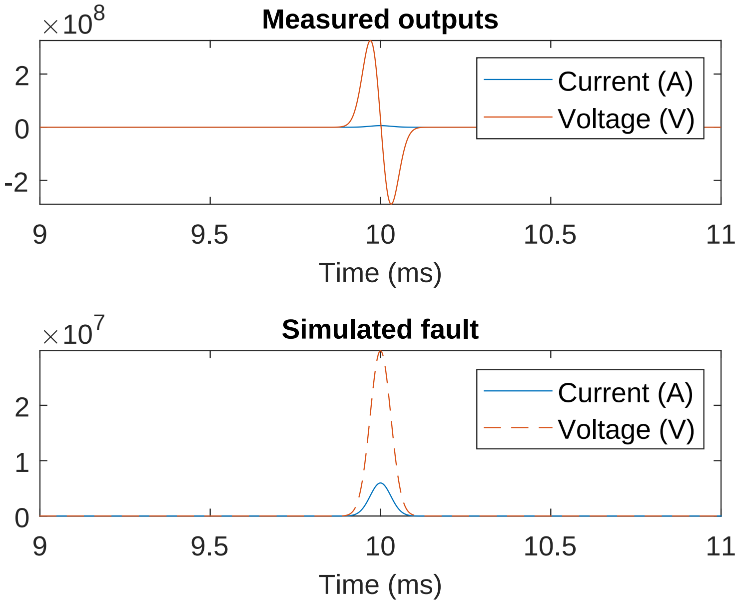

Figure 23: Simulated current and voltage at fault location, together with corresponding sensor outputs.

followed, with bandwidth values as previously stated: $\omega_b = 10\omega_f$ and $\omega_f = 10\omega^\star$. For the red line, the fault bandwidth $\omega_f$ is reduced to a tenth of the critical frequency $\omega^\star$, and for the yellow line, the sensor bandwidth $\omega_b$ is reduced to a tenth of the fault bandwidth. The latter are almost completely uninformative. Focusing on the blue line, its shape suggests that gradient descent will converge to one of two global minima, for any non-zero initial condition. The observed symmetry means that unconstrained optimisation can be employed, if the sign of the result is ignored. For this instance of fault localization problem, given an initial guess of 1 m (i.e., a 1.999 km initial error), MATLAB's `fminunc` returns a location estimate within 4.21 s with a 5.39 cm error. A standard HP Elitebook was used, with Intel CORE i7 vPRO processor and 32 GB RAM, running MATLAB R2022b on Windows 10.

## 5.5 Discussion

In this section, we have introduced three methods for fault distance localization. The first two methods, EMTR and LPSF, are adapted for direct fault localization in the network in Section 5.1. In contrast, the final method based on PDE models is better suited for sampling rate and theoretical feasibility studies.

The EMTR method belongs to the class of traveling wave methods, and is characterized by a need for a high sampling rate and a detailed simulation model of the entire grid. Localization is done by comparing the current's signal energy at hypothesized fault locations. The location with the largest signal energy is the estimated fault position. In contrast, the LPSF method uses a simplified single feeder model with no branches. It assumes a steady state is reached during the fault and does not exploit the transient data leading from the nominal to the faulty state.

As shown in this section, both EMTR and LPSF provide good fault location estimates in many cases. However, both methods struggle with high-ohmic faults since the fault current is so small that reliable estimates are hard to obtain. Both methods also struggle with heterogeneous networks. In the EMTR method, heterogeneity causes wave reflections, which interfere with the actual fault signal. A possible solution is to introduce a second sensor. Optimal placement of additional sensors is a good problem

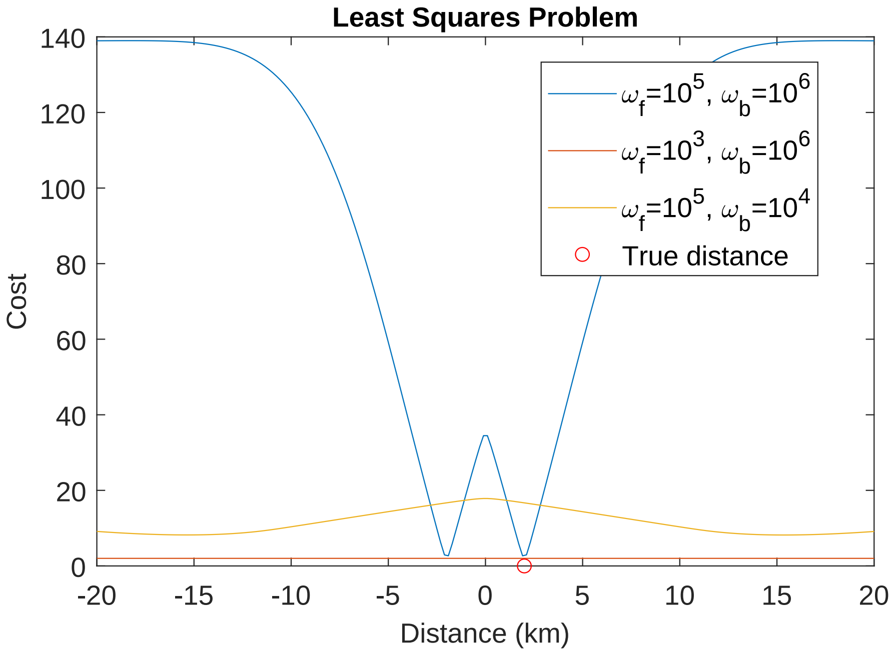

Figure 24: Cost $J(\ell)$ as a function of $\ell$, under different fault and sensor bandwidths. Blue plot: $\omega_f = 10\omega^\star$, $\omega_b = 100\omega^\star$. Red plot: $\omega_f = 0.1\omega^\star$, $\omega_b = 100\omega^\star$. Yellow plot: $\omega_f = 10\omega^\star$, $\omega_b = \omega^\star$. Frequencies are in rad/s.

for future work. Search methods that drive the exploration instead of examining every single fault location can also be explored.

The PDE method can be extended by relaxing the assumption that the fault voltage and impedance is known. This is the subject of ongoing work. For the LPSF method, a possible improvement for heterogeneous networks is introducing piece-wise linear (in fault distance) impedance and admittance models. However, the main point for improvement is the development of a more reliable fault current estimator. Both a model and a data-based current estimator were studied here. The data-based one in (OPT2) was more reliable in the cases considered but struggled when the lines were heterogeneous. For future work, we can consider larger classes of fault current estimators, such as $\hat{I}_{\mathsf{F}}(x, R_{\mathsf{F}}, I_0; \theta)$, where $\theta$ is a vector of weights in a neural network.

# 6 Conclusion

The RESili8 project has made significant strides in redefining resilience for Cyber-Physical Energy Systems (CPESs) in the context of the digital energy transition. Recognizing the limitations of traditional resilience strategies, the project has developed a comprehensive solution package that integrates AI-based analysis, automated validation, and advanced fault localization techniques. These innovations collectively address the multifaceted challenges posed by the increasing complexity, decentralization, and digitalization of modern energy systems.

One of the project's key achievements is the development of a semi-automated AI toolchain that leverages expert knowledge and reinforcement learning to generate realistic threat scenarios and test cases. This toolchain enables faster and more effective validation of energy applications in lab environments, ensuring that critical vulnerabilities are identified and addressed early in the development process. The integration of STPA, MUCs, and HTDs provides a structured and scalable approach to resilience analysis.

The Automated Cyber-Physical Testing and Validation Framework (ACTV) represents another major milestone. By embedding system-level validation into CI/CD pipelines, ACTV facilitates continuous testing of smart grid applications in real-time simulation environments. This approach not only enhances test coverage and reproducibility but also supports collaboration between developers and test service providers across distributed locations.

In the domain of fault localization, RESili8 has conducted a thorough evaluation of three complementary methods—EMTR, LPSF, and PDE-based modeling. Each method offers unique strengths and trade-offs, and their combined insights contribute to a more robust understanding of fault detection in heterogeneous distribution networks. The project's use of real-world data and simulation models has further validated the practical applicability of these techniques.

While the project has delivered substantial technical outcomes, it also highlights areas for future research and development. These include improving the scalability of AI-based analysis, enhancing the accuracy of fault localization in complex networks, and expanding the ACTV framework to support a broader range of applications and test scenarios. The integration of data-driven and model-based approaches remains a promising avenue for further exploration.

In conclusion, RESili8 has laid a strong foundation for the next generation of resilient energy systems. Its contributions extend beyond technical innovations to include methodological frameworks and collaborative practices that can be adopted by stakeholders across the energy sector. As the energy landscape continues to evolve, the principles and tools developed by RESili8 will play a vital role in ensuring the security, reliability, and sustainability of future energy infrastructures.

# Abbreviations

| | |
|---|---|
| ACTV | Automated Cyber-Physical Testing and Validation Framework |
| C-HIL | Controller-HIL |
| EMTR | Electro-Magnetic Time Reversal |
| HIL | Hardware-in-the-Loop |
| HTD | Holistic Test Description |
| LPSF | Lumped Parameter Single Feeder |
| MUC | Misuse Case |
| P-HIL | Power-HIL |
| PDE | Partial Differential Equation |
| RTDS | Real-time Digital Simulator |
| STPA | Systems Theoretic Process Analysis |

# References

[1] Janne Altonen and Ari Wahlroos. Novel algorithm for earth-fault location in compensated MV-networks. In *22nd International Conference and Exhibition on Electricity Distribution (CIRED 2013)*, pages 1–4, June 2013.

[2] A. Borghetti, M. Bosetti, C. A. Nucci, M. Paolone, and A. Abur. Integrated Use of Time-Frequency Wavelet Decompositions for Fault Location in Distribution Networks: Theory and Experimental Validation. *IEEE Transactions on Power Delivery*, 25(4):3139–3146, October 2010. Conference Name: IEEE Transactions on Power Delivery.

[3] Jie Chen, Ron J. Patton, and Hong-Yue Zhang. Design of unknown input observers and robust fault detection filters. *International Journal of Control*, 63(1):85–105, January 1996.

[4] Zhe Chen, Zhaoyang Wang, Mario Paolone, and Farhad Rachidi. Properties of direct-time and reversed-time transfer functions to locate disturbances along power transmission lines. In *2019 IEEE Milan PowerTech*, pages 1–6. IEEE, 2019.

[5] Mehmet Hazar Cintuglu, Osama A. Mohammed, Kemal Akkaya, and A. Selcuk Uluagac. A survey on smart grid cyber-physical system testbeds. *IEEE Communications Surveys & Tutorials*, 19(1):446–464, 2017.

[6] Christian Dänekas, Christian Neureiter, Sebastian Rohjans, Mathias Uslar, and Dominik Engel. Towards a model-driven-architecture process for smart grid projects. In Pierre-Jean Benghozi, Daniel Krob, Antoine Lonjon, and Hervé Panetto, editors, *Digital Enterprise Design & Management*, pages 47–58, Cham, 2014. Springer International Publishing.

[7] Michiel De Nooij, Barbara Baarsma, Gabriël Bloemhof, Han Slootweg, and Harold Dijk. Development and application of a cost–benefit framework for energy reliability: Using probabilistic methods in network planning and regulation to enhance social welfare: The n-1 rule. *Energy Economics*, 32(6):1277–1282, 2010.

[8] Mehdi Dehghan and Ali Shokri. A numerical method for solving the hyperbolic telegraph equation. *Numerical Methods for Partial Differential Equations*, 24(4):1080–1093, 2008.

[9] G. Druml, P. Stachel, S. Gebhard, W. Leitner, O. Skrbinjek, G. Achleitner, U. Schmidt, and P. Schegner. New Method for Measuring the Earthfault-Distance in Compensated and Isolated Networks. In *CIRED 2021 - The 26th International Conference and Exhibition on Electricity Distribution*, volume 2021, pages 1416–1419, September 2021.

[10] G. Druml, P. Stachel, W. Leitner, O. Skrbinjek, U. Schmidt, and P. Schegner. Results from the new method for measuring the earthfault-distance in compensated and isolated networks. In *16th International Conference on Developments in Power System Protection (DPSP 2022)*, volume 2022, pages 13–18, March 2022.

[11] M. El-Hami, L.L. Lai, D.J. Daruvala, and A.T. Johns. A new travelling-wave based scheme for fault detection on overhead power distribution feeders. *IEEE Transactions on Power Delivery*, 7(4):1825–1833, October 1992. Conference Name: IEEE Transactions on Power Delivery.

[12] Catalin Gavriluta, Cedric Boudinet, Friederich Kupzog, Antonio Gomez-Exposito, and Raphael Caire. Cyber-physical framework for emulating distributed control systems in smart grids. *International Journal of Electrical Power & Energy Systems*, 114:105375, 2020.

[13] Farhad Ghanipoor, Carlos Murguia, Peyman Mohajerin Esfahani, and Nathan van de Wouw. Ultra Local Nonlinear Unknown Input Observers for Robust Fault Reconstruction. In *2022 IEEE 61st Conference on Decision and Control (CDC)*, pages 918–923, December 2022. ISSN: 2576-2370.

[14] J. Duncan Glover, Mulukutla S. Sarma, Thomas Overbye, and Adam Birchfield. *Power System Analysis and Design, SI Edition*. Cengage Learning, 7 edition, March 2022.

[15] J.D. Glover, M.S. Sarma, and T. Overbye. *Power System Analysis and Design*. Cengage Learning, 2011.

[16] M. Z. Habib. *Fault location in resonant earthed medium voltage distribution systems*. PhD dissertation, KTH Royal Institute of Technology, Stockholm, Sweden, 2022.

[17] Zakaria Habib. *Fault location in resonant earthed medium voltage distribution systems*. PhD Thesis, KTH Royal Institute of Technology, Stockholm, 2022. ISBN 978-91-8040-434-1.

[18] Bill Haskins, Jonette Stecklein, Brandon Dick, Gregory Moroney, Randy Lovell, and James Dabney. 8.4.2 error cost escalation through the project life cycle. *INCOSE International Symposium*, 14(1):1723–1737, 2004.

[19] Shaoyin He, Andrea Cozza, and Yan-zhao Xie. Electromagnetic time reversal as a correlation estimator: Improved metrics and design criteria for fault location in power grids. *IEEE Transactions on Electromagnetic Compatibility*, 62(2):598–611, 2019.

[20] Seppo Hänninen and Matti Lehtonen. *Earth fault distance computation with fundamental frequency signals based on measurements in substation supply bay*. VTT Tiedotteita. Valtion Teknillinen Tutkimuskeskus, Espoo, 2002.

[21] Mehrdad Lakestani and Behzad Nemati Saray. Numerical solution of telegraph equation using interpolating scaling functions. *Computers & Mathematics with Applications*, 60(7):1964–1972, October 2010.

[22] Georg Lauss and Kai Strunz. Accurate and stable hardware-in-the-loop (hil) real-time simulation of integrated power electronics and power systems. *IEEE Transactions on Power Electronics*, 36(9):10920–10932, 2021.

[23] Rui Liang, Guoqing Fu, Xueyuan Zhu, and Xue Xue. Fault location based on single terminal travelling wave analysis in radial distribution network. *International Journal of Electrical Power & Energy Systems*, 66:160–165, March 2015.

[24] Yuan Liu, Renke Huang, Wei Du, Ankit Singhal, and Zhenyu Huang. Highly-scalable transmission and distribution dynamic co-simulation with 10,000+ grid-following and grid-forming inverters. *IEEE Transactions on Power Delivery*, 39(1):578–590, 2024.

[25] Christoph Mayer, Gert Brunekreeft, Marita Blank-Babazadeh, Sanja Stark, Marius Buchmann, Mathias Dalheimer, et al. Resilienz digitalisierter energiesysteme. *Blackout-Risiken Verstehen, Stromversorgung Sicher Gestalten*, 2020.

[26] R. K. Mohanty, Bishnu Pada Ghosh, and Gunjan Khurana. High-precision numerical method for 1D quasilinear hyperbolic equations on a time-graded mesh: application to Telegraph model equation. *Soft Computing*, March 2023.

[27] Tung-Lam Nguyen, Yu Wang, Quoc-Tuan Tran, Raphael Caire, Yan Xu, and Catalin Gavriluta. A distributed hierarchical control framework in islanded microgrids and its agent-based design for cyber–physical implementations. *IEEE Transactions on Industrial Electronics*, 68(10):9685–9695, 2021.

[28] Shreya Parmar. Fault Location Algorithms for Electrical Power Transmission Lines. Master's thesis, Delft University of Technology, Delft, July 2015.

[29] Reza Razzaghi, Gaspard Lugrin, Hossein Manesh, Carlos Romero, Mario Paolone, and Farhad Rachidi. An efficient method based on the electromagnetic time reversal to locate faults in power networks. *IEEE Transactions on Power Delivery*, 28(3):1663–1673, 2013.

[30] Abbas Saadatmandi and Mehdi Dehghan. Numerical solution of hyperbolic telegraph equation using the Chebyshev tau method. *Numerical Methods for Partial Differential Equations*, 26(1):239–252, 2010.

[31] Henrik Sandberg, Victor Bagge, Diego Cifelli, and Daniel Selvaratnam. RESili8 Deliverable D5.2 – Anomaly Detection and Identification. Technical report, ERA-Net RESili8, June 2024.

[32] Johann Schütz, Mathias Uslar, and Marie Clausen. *Digitalisierung. Synthesebericht 3 des SINTEG Förderprogramms, Studie im Auftrag des BMWK, Berlin*. Berlin, 05 2022.

[33] Daniel Selvaratnam, Amritam Das, and Henrik Sandberg. Electrical Fault Localisation Over a Distributed Parameter Transmission Line. In *2023 62nd IEEE Conference on Decision and Control (CDC)*, pages 7088–7093, December 2023.

[34] Fatemeh Mohammadi Shakiba, Milad Shojaee, S. Mohsen Azizi, and Mengchu Zhou. Real-Time Sensing and Fault Diagnosis for Transmission Lines. *International Journal of Network Dynamics and Intelligence*, pages 36–47, December 2022.

[35] Shokofeh Sharifi and Jalil Rashidinia. Numerical solution of hyperbolic telegraph equation by cubic B-spline collocation method. *Applied Mathematics and Computation*, 281:28–38, April 2016.

[36] Sachin Shivakumar, Declan Jagt, Danilo Braghini, Amritam Das, and Matthew Peet. PIETOOLS 2022: User Manual, December 2022. arXiv:2101.02050 [math].

[37] K. Strunz, Ehsan Abbasi, Robert Fletcher, Nikos Hatziargyriou, Reza Iravani, and Géza Joos. *TF C6.04.02 : TB 575 – Benchmark Systems for Network Integration of Renewable and Distributed Energy Resources*. 04 2014.

[38] Anton Thorslund. Swedish Transmission Grid Model Based on Open Sources. Master's thesis, Chalmers University of Technology, 2017.

[39] Mathias Uslar. Energy Informatics: Definition, State-of-the-art and new horizons. In Friederich Kupzog, editor, *Proceedings der ComForEn 2015 Vienna*, Wien, 2015. TU Wien, OVE Verlag.

[40] Mathias Uslar, Sebastian Rohjans, Christian Neureiter, Filip Pröstl Andrén, Jorge Velasquez, Cornelius Steinbrink, Venizelos Efthymiou, Gianluigi Migliavacca, Seppo Horsmanheimo, Helfried Brunner, et al. Applying the smart grid architecture model for designing and validating system-of-systems in the power and energy domain: A european perspective. *Energies*, 12(2):258, 2019.

[41] Zhaoyang Wang, Shaoyin He, Reza Razzaghi, Mario Paolone, Yanzhao Xie, and Farhad Rachidi. A review of time reversal-based methods applied to fault location in power networks. *Frontiers in Energy Research*, 10:1060938, 2022.

[42] Zhaoyang Wang, Reza Razzaghi, Mario Paolone, and Farhad Rachidi. Time reversal applied to fault location in power networks: Pilot test results and analyses. *International Journal of Electrical Power & Energy Systems*, 114:105382, 2020.

[43] Arlena Wellßow, Paul Smith, Edmund Widl, Eric Veith, Julian Kohlisch-Posega, Francesca Soro, Malte Puhan, Andreas Theil, Mathias Uslar, and Roland Zoll. Machine-readable expert knowledge representation concept, 2024.

[44] Arlena Wellßow and Eric MSP Veith. Power switch: Online vs. offline learning in the energy domain.

[45] Arlena Wellßow, Torben Logemann, and Eric MSP Veith. Trajectory generation model: Building a simulation link between expert knowledge and offline learning. In *International Conference on Simulation and Modeling Methodologies, Technologies and Applications (SIMULTECH)(accepted)*, 2024.

[46] Arlena Wellßow, Paul Smith, Oliver Jung, and Edmund Widl. RESili8 Deliverable D4.3 – AI-Based Analysis and Evaluation Approach. Technical report, ERA-Net RESili8, May 2025.

[47] Yiqi Xing, Yu Liu, Dayou Lu, Xinchen Zou, and Xuming He. A Physics-Informed Data-Driven Fault Location Method for Transmission Lines Using Single-Ended Measurements with Field Data Validation, July 2023. arXiv:2307.09740 [cs, eess].

[48] Rajaa Vikhram Yohanandhan, Rajvikram Madurai Elavarasan, Rishi Pugazhendhi, Manoharan Premkumar, Lucian Mihet-Popa, Junbo Zhao, and Vladimir Terzija. A specialized review on outlook of future cyber-physical power system (cpps) testbeds for securing electric power grid. *International Journal of Electrical Power & Energy Systems*, 136:107720, 2022.

[49] Claudia Zanabria, Filip Pröstl Andrén, and Thomas I. Strasser. Comparing specification and design approaches for power systems applications. In *2018 IEEE PES Transmission & Distribution Conference and Exhibition - Latin America (T&D-LA)*, pages 1–5, 2018.

## CONSORTIUM

## DISCLAIMER

## COPYRIGHT

This project has received funding in the framework of the joint programming initiative ERA-Net Smart Energy Systems' focus initiative Digital Transformation for the Energy Transition, with support from the European Union's Horizon 2020 research and innovation programme under grant agreement No 883973.